POLITECNICO DI TORINO
Repository ISTITUZIONALE

Functionally graded IN718-WC composites cladding on 17-4 ph martensitic stainless steel via laser powder bed fusion additive manufacturing

Original
Functionally graded IN718-WC composites cladding on 17-4 ph martensitic stainless steel via laser powder bed fusion additive manufacturing / Imani, H., Naffakh-Moosavy, H., Taghian, M., Saboori, A., Iuliano, L.. - In: RESULTS IN ENGINEERING. - ISSN 2590-1230. - 30:(2026). [10.1016/j.rineng.2026.109873]

Availability:
This version is available at: 11583/3012825 since: 2026-07-08T10:17:42Z

Publisher:
Elsevier B.V.

Published
DOI:10.1016/j.rineng.2026.109873

Terms of use:

This article is made available under terms and conditions as specified in the corresponding bibliographic description in the repository

Publisher copyright

(Article begins on next page)

29 November 2026

Results in Engineering 30 (2026) 109873

Contents lists available at ScienceDirect

Results in Engineering

journal homepage: www.sciencedirect.com/journal/results-in-engineering

Research paper

Functionally graded IN718-WC composites cladding on 17-4 ph martensitic stainless steel via laser powder bed fusion additive manufacturing

Hadise Imani [a], Homam Naffakh-Moosavy [a,*], Mohammad Taghian [b,c], Abdollah Saboori [b,c], Luca Iuliano [b,c]

[a] Department of Materials Engineering, Tarbiat Modares University (TMU), Tehran, Iran
[b] Department of Management and Production Engineering, Politecnico di Torino, Torino, Italy
[c] Integrated Additive Manufacturing Center, Politecnico di Torino, Torino, Italy

ARTICLE INFO

Keywords:
Additive Manufacturing
Laser Powder Bed Fusion
IN718/WC Composite
Functionally Graded Materials
17-4PH Martensitic Stainless Steel
Wear

ABSTRACT

Inconel 718 (IN718) is widely used in cladding applications due to its excellent high-temperature strength, but its relatively low hardness and limited wear resistance reduce its functional performance. Incorporating tungsten carbide (WC) as a reinforcing phase can improve mechanical properties, though its high hardness and melting point present challenges for conventional cladding techniques. In this study, IN718-based composite clads reinforced with 20 wt.% WC were fabricated on a 17-4PH martensitic stainless steel substrate using Laser Powder Bed Fusion (L-PBF), and the effects of compositional grading on microstructure and mechanical performance were investigated. Three clad architectures were designed: a non-graded sample (NG-20), a graded sample with 5 wt.% WC increments (G-5), and a graded sample with 10 wt.% WC increments (G-10). Characterization included X-ray diffraction (XRD), optical and scanning electron microscopy (SEM), Vickers microhardness testing, and wear testing at room temperature and 350 °C using AISI 52100 steel pins. The primary phases identified were an austenitic γ-matrix, WC particles, and Laves phase, with in situ interfacial reactions forming diffusion layers around WC particles. Graded samples exhibited more uniform WC distribution and reduced porosity (<0.5%) compared to the non-graded sample (0.9%). All composite clads showed increased hardness, with NG-20, G-5, and G-10 increasing by 74%, 79%, and 91%, respectively. Wear tests revealed G-5 achieved the highest wear resistance, reducing wear rates by 38% and 42% at room temperature and 350 °C, respectively. G-10 reductions were 19% and 30%, and NG-20 reductions were 18% and 25%. Overall, the G-5 sample was identified as the optimal configuration, combining low porosity with enhanced mechanical performance.

1. Introduction

Stainless steels are widely used in industries such as turbine manufacturing, power generation, and oil refining due to their excellent corrosion resistance, cost-effectiveness, and relatively low density [1–3]. Similarly, nickel-based superalloys are extensively employed in high- performance applications, including coatings for industrial gas turbines, aircraft engines, and critical components in nuclear reactors (e.g., blades, vanes, turbine disks, and combustion chambers), owing to their remarkable high-temperature strength, oxidation resistance, and resistance to wear and hot corrosion [4–7]. However, despite these advantages, Inconel 718 superalloy exhibits limited hardness and wear resistance, which restricts its suitability for demanding industrial applications. To address these limitations, metal matrix composites (MMCs) reinforced with ceramic particles have gained attention in commercial applications due to their superior performance-to-cost ratio, ease of fabrication, and environmentally friendly characteristics. Incorporating ceramic reinforcements such as titanium carbide (TiC), tungsten carbide (WC), and chromium carbide (CrC) into nickel-based alloys significantly enhances their strength, hardness, and wear resistance [8,9]. Among these reinforcements, tungsten carbide (WC), due to its high hardness and excellent creep resistance at elevated temperatures, has attracted significant attention and is commonly added to nickel-based matrices to enhance wear properties [10,32]. Compared to advanced additive manufacturing techniques, conventional methods such as casting, powder metallurgy, and in-situ sintering may, under specific conditions, face challenges including higher production costs and increased tool wear [11].

* Corresponding author.
E-mail address: h.naffakh-moosavy@modares.ac.ir (H. Naffakh-Moosavy).

https://doi.org/10.1016/j.rineng.2026.109873
Received 2 November 2025; Received in revised form 28 January 2026; Accepted 2 March 2026
Available online 18 March 2026
2590-1230/© 2026 Published by Elsevier B.V. This is an open access article under the CC BY-NC-ND license (http://creativecommons.org/licenses/by-nc-nd/4.0/).

Laser Powder Bed Fusion (L-PBF), an advanced additive manufacturing (AM) technique, has emerged as a promising technology for fabricating complex geometries with near-full density, high dimensional accuracy, refined microstructures, and excellent mechanical properties. In contrast, laser powder bed fusion (LPBF) is recognized as an advanced manufacturing technique for fabricating complex components with near-full density, high dimensional accuracy, optimized microstructures, and superior mechanical properties. Owing to the formation of extremely small melt pools and ultra-high cooling rates, LPBF enables the production of components with enhanced chemical homogeneity and refined grain structures, which play a critical role in improving the overall performance of metallic materials [11–14,33]. For instance, Ting Rong and colleagues employed the L-PBF process to fabricate Inconel 718 composites reinforced with WC_{1-x} particles. They investigated the influence of laser energy density on the density, particle dispersion, and microstructure. Their results showed that under an optimal energy density of 242 J/m, the fabricated part exhibited high hardness (389.4 $HV_{0.1}$), a low friction coefficient (0.39), and reduced wear rates [15]. Likewise, Yongkang Gao et al. studied WC/IN718 composites with varying WC content (10–20 wt.%). The addition of WC particles led to uniform particle distribution, strong metallurgical bonding, and the formation of a layered microstructure (WC-W_2C/M_xC/IN718). Hardness increased from 304.8 HV to 421.3 HV with increasing WC content, while wear resistance peaked at 15 wt.% WC [16]. Furthermore, Hongmei Zhang et al. introduced nanoscale WC particles into IN718 alloy using the Laser Powder Bed Fusion (L-PBF) technique, successfully fabricating composites reinforced with carbide and oxide nanoparticles. The addition of 2 wt.% WC promoted the precipitation of carbides and oxides, refined the grain structure, and increased dislocation density. These improvements resulted in a 28.8% increase in yield strength and a 26.5% rise in ultimate tensile strength, while maintaining excellent ductility [17]. Composites offer advantages over pure metals or alloys, including superior strength, fatigue resistance, and improved wear and corrosion resistance. However, a key challenge in using these materials lies in the abrupt change in properties at the interfaces between dissimilar parts, which can result in delamination and failure under severe operating conditions. To overcome this issue, the concept of functionally graded materials (FGMs) was introduced in 1972. Inspired by the natural structure of materials, such as bone and bamboo, FGMs aim to enhance mechanical properties and optimize material performance. First used in 1984 in Japan for space shuttle design, FGMs have since been recognized as an effective strategy for controlling material behavior under deformation, dynamic loading, corrosion, and wear.

Additionally, FGMs serve as effective intermediate layers for joining dissimilar materials, significantly mitigating interfacial issues. In this context, Directed Energy Deposition (DED) is among the most popular AM methods for producing FGMs due to its ability to vary material composition during fabrication through controlled powder feeding. However, DED has inherent limitations, including insufficient resolution for fabricating complex geometries, extensive post-processing requirements, low powder utilization efficiency, and difficulty in controlling composition when using powders with differing flow characteristics. Conversely, powder bed fusion (PBF) methods such as L-PBF have emerged as effective alternatives, offering near-net-shape fabrication of high-performance components, combining superior resolution, excellent surface finish, and the ability to produce intricate geometries suitable for demanding service conditions. Despite these advantages, the application of L-PBF for producing FGMs remains in its early stages of development. Research in this area has been relatively sparse, primarily focusing on simple designs, such as bimetallic parts [18–22,34]. Demir et al. developed an L-PBF system capable of in-situ mixing of two metallic powders. Their study demonstrated the feasibility of producing Fe/Al-12Si parts, successfully fabricating multi-layer structures comprising Fe, Fe/Al-12Si, and Al-12Si layers [23]. Likewise, Ghavanati et al. explored the capability of L-PBF to fabricate SS316L-IN718 FGMs. They achieved a high-density part with minimal defects and demonstrated a gradient design featuring a 50 wt.% intermediate region yielded optimal mechanical properties, including a tensile strength of 610 MPa and an elongation of 31.5% [24]. Yang et al. fabricated WC/316L stainless steel gradient layered structures using laser powder bed fusion (LPBF) to achieve a synergistic combination of strength and ductility. Compared with homogeneous 316L stainless steel, the gradient structures exhibited an increase in ultimate tensile strength of approximately 14% for 3 wt.% WC and 18% for 5 wt.% WC, while maintaining an elongation of over 50%. The ultimate tensile strength of the gradient specimens reached 800–850 MPa, demonstrating that the gradient layered design effectively enhances strength without significantly compromising ductility [35].

In this study, a 17-4PH martensitic stainless steel substrate was integrally clad with a composite IN718/20%WC clad layer using the L-PBF process. Three sample architectures were fabricated: one non-graded clad and two compositionally graded clads, in which the WC content varied incrementally by 5% and 10%, respectively. Metallographic characterization, microhardness measurements, and wear testing were performed to evaluate the influence of compositional grading on the microstructure and mechanical properties of the clads.

2. Materials and methods

In this study, 17-4PH martensitic stainless steel was used as the substrate material in the form of gas-atomized spherical powders with an average particle size of 15–45 μm. Nickel-based superalloy IN718 and tungsten carbide (WC) served as the main components for the laser-cladded functionally graded composite structures. Gas-atomized IN718 powder (15–45 μm) and WC powder (0–5 μm) were blended via mechanical mixing in ceramic containers for 24 hours, without the use of milling media, and the mixed powder was dried in an oven at 100°C for 2 hours. X-ray fluorescence (XRF) spectroscopy analysis of IN718 and 17-4PH powders is provided in Table 1, while the morphologies of the IN718, WC, and 17-4PH powders are shown in Fig. 1.

The fabrication was carried out using a Concept Laser MLab Cusing R machine, equipped with a 100 W Nd: YAG laser. An argon atmosphere was employed to control the oxygen concentration within the build chamber, keeping it below 0.2%. The detailed process parameters, which were selected based on prior experience with each powder type, are listed Table 2.

A 6 mm-thick 17-4PH martensitic stainless steel substrate was fabricated via L-PBF process, followed by the deposition of a 1 mm-thick cermet coating composed of IN718 reinforced with 20 wt.% WC using the same method. To investigate the influence of compositional grading on solidification behavior, microstructural evolution, and mechanical properties, three sample configurations were designed: (1) a non-graded structure comprising five uniform layers of IN718 + 20 wt.% WC; (2) a graded structure with 5 wt.% WC increments across five layers, transitioning from pure IN718 to IN718 + 20 wt.% WC; and (3) a graded structure with 10 wt.% WC increments, consisting of one layer of pure IN718, followed by two layers of 90/10, and two layers of 80/20 composition. For wear testing, disk-shaped samples with a diameter of 30 mm and a total thickness of 7 mm (including the substrate and coating) were prepared. For the graded composites, the powder for each layer was prepared with the desired WC content via mechanical mixing, deposited using the LPBF process, and the surface was cleaned before the

Table 1
Chemical composition of SS 17-4PH and IN718 powders (wt.%).

SS 17-4PH						
Fe	Cr	Ni	Cu	Nb+Ta	C	Others
Balance	17	4.5	4.0	0.3	<0.07	<1.0
IN718						
Ni	Fe	Cr	Nb	Mo	Ti	Al
Balance	18.07	18.49	5.38	3.21	1.03	0.6

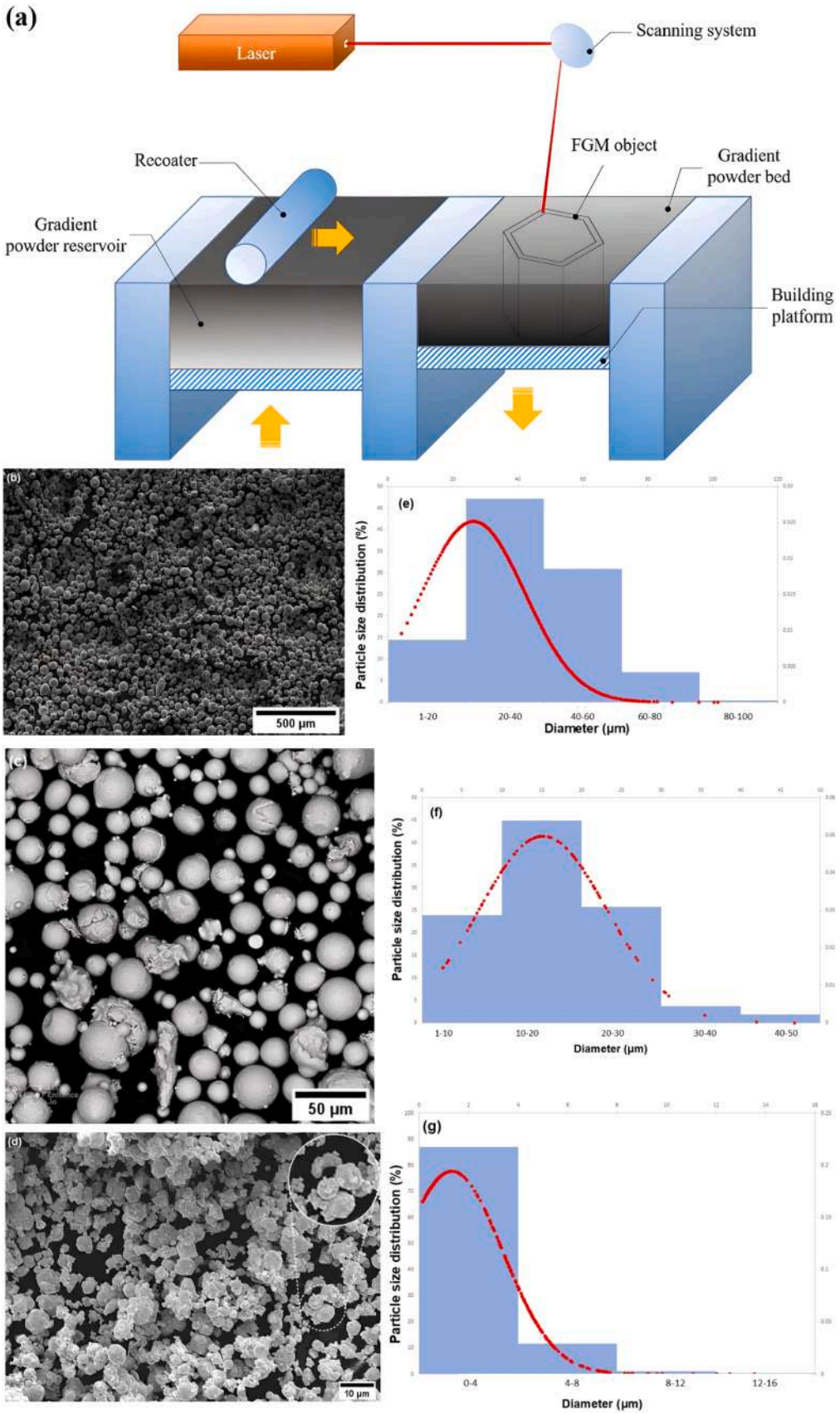

Fig. 1. Manufacturing procedure of IN718/WC FGMs: a) Conceptual schematic of the standard L-PBF system assigned to fabricate FGMs. SEM image of (b) SS17-4PH, (c) IN718, and (d) WC powder; Particle size distribution of (e) SS17-4PH, (f) IN718, and (g) WC.

Table 2
Parameters of the L-PBF process.

parameters	17-4PH	IN718/WC
Power [W]	95	95
Scan Speed [mm/s]	400	800
Hatch Distance [mm]	0.084	0.05
Layer thickness [mm]	0.025	0.025
Volumetric Energy Density [J/mm^3]	94	95
Scanning Strategy	Stripe/67°	Stripe/67°

next layer was applied; this procedure was repeated until the final graded structure was obtained.

Fig. 2 illustrates the schematic representation of the fabricated samples. The FGM samples were subjected to a series of experimental characterizations as illustrated in Fig. 2. Phase compositions were analyzed by X-ray diffraction (XRD) on both the surface and the substrate. Electrochemical polishing of the samples was performed in a solution of 94 vol.% CH_3COOH and 6 vol.% $HClO_4$ at 50 V for 10 seconds to ensure surface quality. Optical microscopy (OM) was used to assess the macro- and microstructures, and image analysis was conducted using ImageJ software. Porosity was measured using optical microscopy on etched samples. For each sample, nine regions at a specific magnification were selected to distinguish pores from WC particles, and ImageJ software was used to quantify the porosity. For a more detailed investigation, scanning electron microscopy (SEM) equipped with energy-dispersive X-ray spectroscopy (EDS) was employed. Vickers microhardness testing was performed under a load of 100 gf and a dwell time of 15 seconds, with three measurements conducted at each layer and the average reported. Indentations were placed within the metallic matrix using the optical microscope of the tester to avoid direct interaction with WC particles. To evaluate wear performance and the effect of compositional grading, pin-on-disk wear tests were conducted following ASTM G99. Testing conditions included a 220 N load, 50 rpm speed, and 7 mm wear track radius, sustained over 4 hours. Tests were carried out at both room temperature and 350 °C using an AISI 52100 steel pin (60 HRC, 5 mm radius) sliding against the prepared disks. Post-test SEM analysis was used to characterize the wear mechanisms.

3. Results and discussion

3.1. XRD Phase analysis

XRD analysis of the 17-4PH stainless steel (Fig. 3) indicated that the microstructure predominantly consists of martensite along with retained austenite. Some diffraction peaks overlapped with ferrite due to the structural similarity between martensite and ferrite. The high heating and cooling rates in additive manufacturing limit the complete transformation of δ-ferrite into more stable phases like martensite or austenite. Alloying elements such as nickel enhance the stability of austenite, preventing its full transformation. Retained austenite can improve toughness and wear resistance, while δ-ferrite may increase hardness but reduce toughness if present in large amounts. The high hardness of the sample confirms the predominance of martensite.

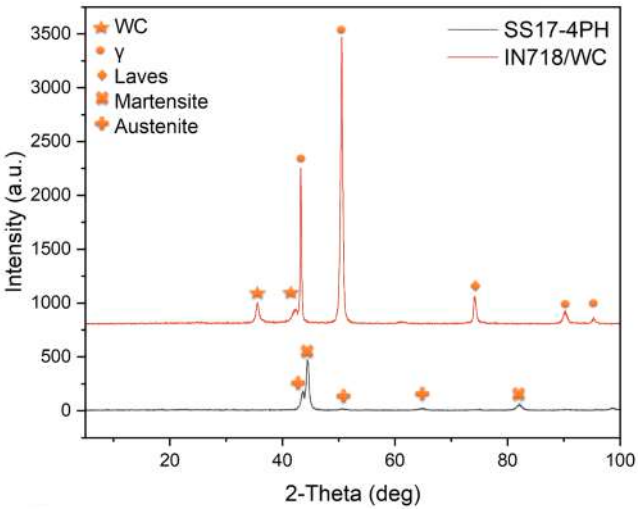

Fig. 3. X-ray diffraction (XRD) patterns obtained from the surface of the composite cladding and the 17-4PH stainless steel substrate.

The XRD pattern of the IN718+20%WC composite clads (Fig. 3), recorded over a wide 2θ range of 30°–100°, has firm diffraction peaks corresponding to the γ-phase (Ni-Cr-Fe matrix), along with weaker peaks associated with the reinforcing WC particles. In general, the phases identified in the samples fabricated via the L-PBF process include the matrix phase, WC, and the Laves phase. The absence of γ′ and γ″ strengthening phases in the XRD pattern is primarily due to the consumption of niobium (Nb) during the formation of the Laves phase, which inhibits the precipitation of these strengthening phases. Additionally, the thermal energy supplied during the scanning of subsequent layers in the L-PBF process is insufficient to provide the necessary driving force for the nucleation and growth of γ′ and γ″ phases. Consequently, no distinct diffraction peaks corresponding to γ′ and γ″ phases

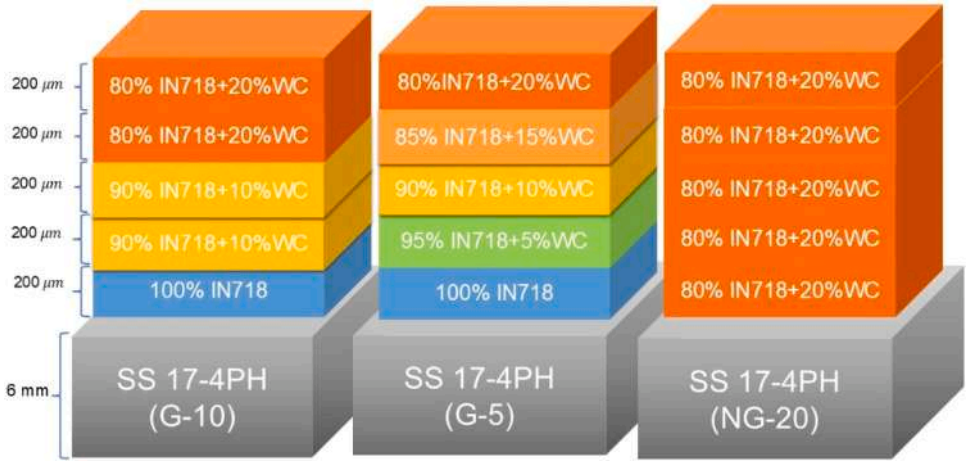

Fig. 2. Schematic illustration of the LPBF fabrication strategy for IN718/WC composite claddings on the 17-4PH stainless steel substrate. The schematic shows the designed coating architectures, including the non-graded (NG-20) and graded (G-5 and G-10) structures. the total cladding thickness is 1 mm, composed of five layers with a nominal thickness of 200 μm each. Dimensions are not to scale and are provided for illustrative purposes only.

are observed in the XRD analysis.

3.2. Evaluation of macrostructure and microstructure

Fig. 4 shows the microstructure of the 17-4PH stainless steel sample fabricated by the L-PBF process, featuring a distinctive circular pattern caused by the hemispherical melt pool shape when viewed from above. Higher magnification (Fig. 4b) reveals strands of delta-ferrite, resulting from rapid heating and cooling rates that limit its transformation into austenite. Due to fast thermal cycles, delta-ferrite grains pass quickly through the austenite stability range, preventing full transformation. While moderate cooling rates promote austenite nucleation by providing sufficient driving force, excessively rapid cooling reduces atomic diffusion and thus hinders nucleation and growth. The samples were produced using a strip scan strategy at a 67° angle, and microstructural analysis was performed on cross-sectional specimens perpendicular to the build direction.

The cross-sectional macrostructure of the IN718+WC composite clads (Fig. 5) reveals the presence of hemispherical melt pools. In the NG-20 sample, the average melt pool width and depth were 87.21 ± 0.01 μm and 60.18 ± 0.98 μm, respectively, which are greater than those of the gradient samples. In the G-5 sample, the average melt pool width and depth were 67.1 ± 0.1 μm and 32.74 ± 0.01 μm, respectively, while in the G-10 sample, the average melt pool width and depth were 86.1 ± 0.1 μm and 37.64 ± 0.71 μm, respectively. As the WC content increased, the clad layers appeared darker in response to the etching solution. The increase in WC content leads to enlarged melt pools due to higher melt viscosity, reduced fluidity, and partial or surface melting of WC particles. Given their high density and melting point, WC particles absorb more laser energy, resulting in an increased adequate melt volume and larger melt pools. In addition, quantitative image analysis of OM micrographs using Image J software revealed that the average WC particle size after fabrication was approximately 5.7 ± 0.6 μm for NG-20, 5.2 ± 0.8 μm for G-10, and 3.7 ± 0.5 μm for G-5. This indicates that the graded G-5 structure promotes a finer and more uniform dispersion of WC particles within the IN718 matrix, which can be attributed to the gradual compositional transition and more stable melt pool dynamics during LPBF processing.

Another notable feature in the structure is the presence of pores with varying sizes and volume fractions in all three samples. As summarized in Table 3, the porosity analysis indicates that compositional gradient design significantly reduces porosity in clads. The NG-20 sample exhibited the highest porosity (0.9%), likely due to (1) reduced melt pool fluidity associated with the high WC content and (2) thermal stresses arising from the mismatch in thermal expansion coefficients between WC particles and the IN718 matrix. Similar trends were reported by Yongkang Gao et al. [16]. The G-5 sample, featuring a 5% WC gradient increment, showed the lowest porosity (0.32%), which can be attributed to a more gradual material transition, improved stress distribution, and better interlayer bonding. In comparison, the G-10 sample, with a 10% WC increment, has slightly higher porosity (0.4%) compared to the G-5 sample, as the more abrupt compositional changes induced localized stresses and negatively impacted interlayer bonding. These results demonstrate that finer compositional gradients are more effective in enhancing density and reducing porosity in composite clads.

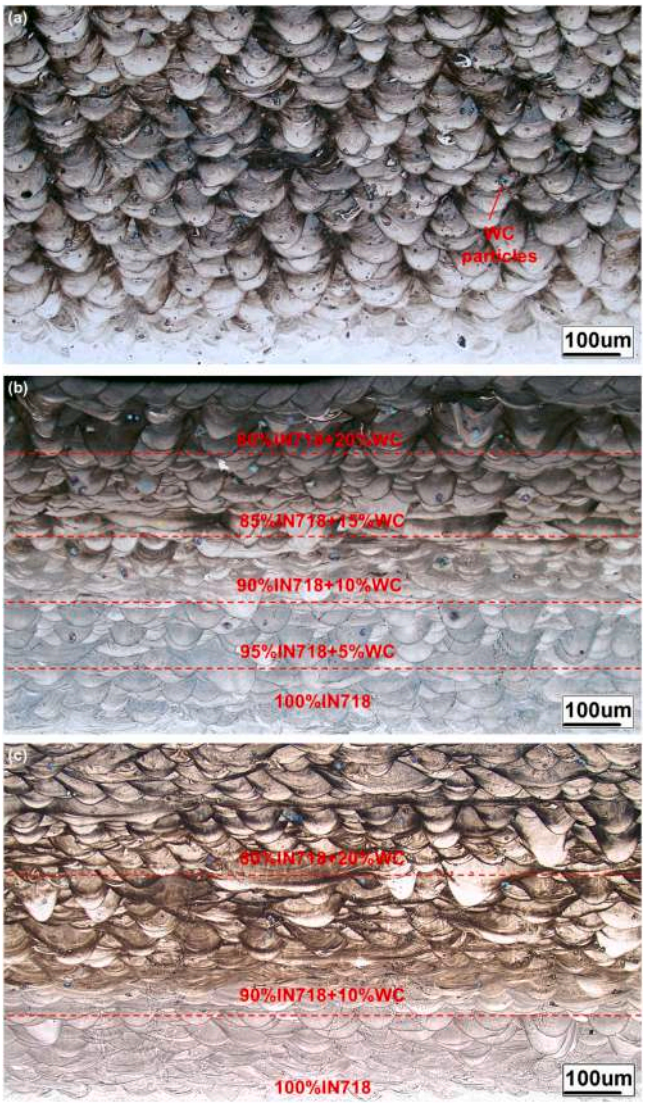

Fig. 5. Optical microscopy images of the macrostructure of the composite clads: (a) NG-20, (b) G-5, and (c) G-10, showing melt pool morphology and the effect of compositional grading on the clad structure.

Fig. 6 presents SEM images of the composite clads. In Fig. 6a, a broader view of the microstructure is shown, revealing the layered melt

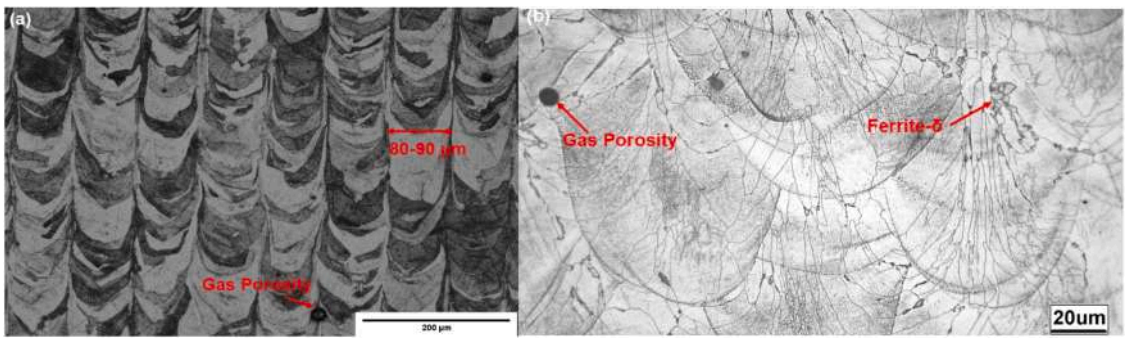

Fig. 4. Optical microscope images of the 17-4PH martensitic stainless steel substrate: (a) macrostructure showing the melt pool morphology, and (b) microstructure.

Table 3
The results of porosity volume fraction measurements.

Sample	Value (%)
Substrate	0.5±0.2
NG-20	0.9±0.1
G-5	0.32±0.12
G-10	0.4±0.1

pools aligned along the build direction. The boundaries of these melt pools, highlighted in the image, represent the interfaces between solidified regions and remelted material resulting from laser passes. Within these zones, both cellular structures and columnar dendrites are visible. Additionally, the presence of the Laves phase is evident in the interdendritic regions. Fig. 7 illustrates the microstructural morphology and the results of linear energy-dispersive spectroscopy (EDS) analysis in the interdendritic regions of the middle layer of the cladding. The results indicate that Nb and Mo are enriched in these regions, whereas the three major elements Ni, Fe, and Cr exhibit no significant variation across the microstructure. During the solidification process, as γ dendrites or cells grow as the primary phase, elements with a partition coefficient less than unity—such as Nb, Ti, C, and Mo—are rejected into the remaining liquid. The enrichment of the liquid with these elements promotes the formation of secondary phases, ultimately leading to the precipitation of the Laves phase via the eutectic reaction $L \rightarrow \gamma + \text{Laves}$. Fig. 6b displays columnar dendritic structures with a PDAS (Primary Dendrite Arm Spacing) of 0.41 ± 0.02 μm, formed at melt pool boundaries due to higher thermal gradients and rapid solidification rates. These conditions favor directional dendrite growth along the thermal gradient.

In contrast, Fig. 6c shows a honeycomb-like cellular structure with a cell size of 0.24 ± 0.08 μm. This morphology forms in regions with more uniform temperature gradients and stable cooling, promoting equiaxed or cellular growth. Fig. 6d presents finer columnar dendrites with a PDAS of 0.21 ± 0.08 μm, where the higher cooling rate limits dendrite growth, resulting in finer structures. The reported PDAS values in Fig. 6 are averaged measurements taken across the entire clads rather than from specific localized zones. This distribution of dendrite spacings reflects local variations in melt pool dynamics, underscoring the influence of cooling rate on the final microstructure. The solidification rate directly governs PDAS. Hunt proposed a model for estimating the cooling rate based on quantitative analysis of PDAS, as shown in Equation (1) [25].

$$\lambda = a\varepsilon^{-b} \tag{1}$$

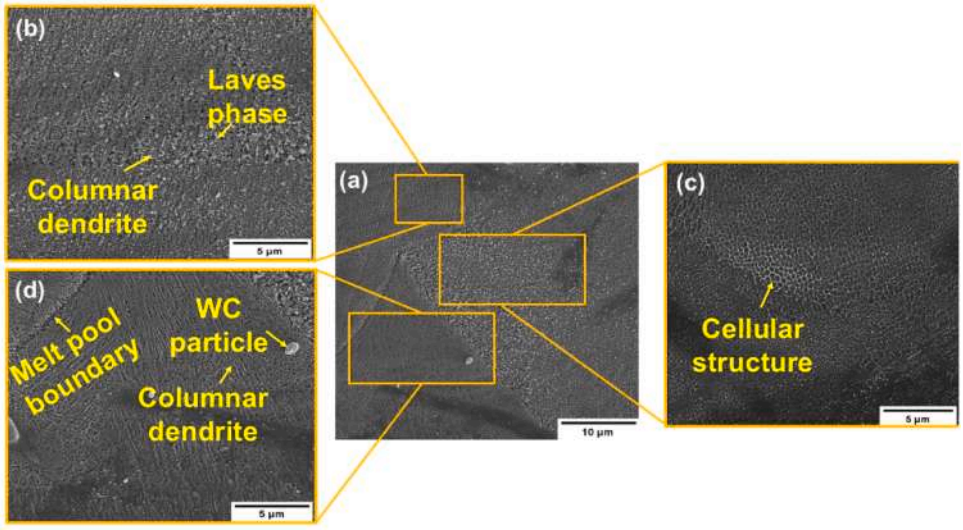

Fig. 6. SEM images of the IN718/WC composite: (a) an overview of the sample's microstructure; (b) a cellular honeycomb structure observed in the marked region of image (a); (c) Laves phase and columnar dendrites located in another designated area in image (a); and (d) columnar dendrites, melt pool boundary, and a tungsten carbide particle as indicated in image (a).

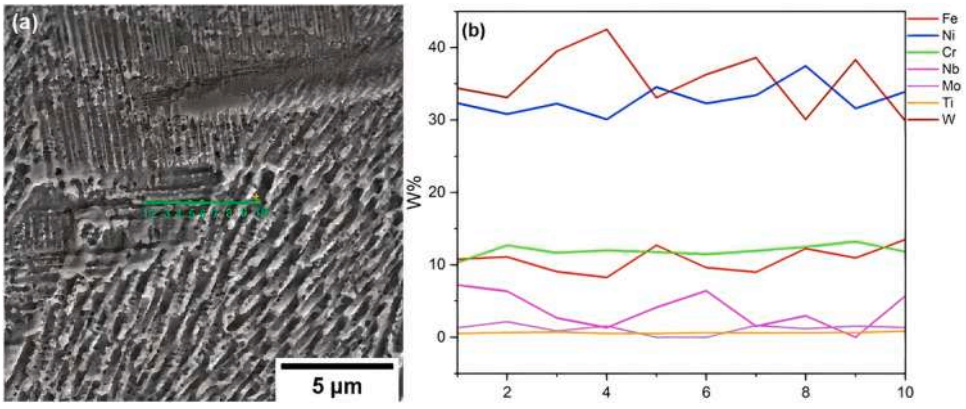

Fig. 7. SEM image and EDS line scan results across the interdendritic regions of the composite cladding, showing the presence of the Laves phase and elemental distribution.

In Equation 1, λ represents the PDAS, while *a* and *b* are material-dependent constants, and ε denotes the cooling rate. For nickel-based superalloys, the constant *a* is approximately 50 μm (K/s), and *b* is typically 0.33. The average cooling rate for each of the three composite samples was calculated and summarized in Table 4. According to Table 4, the NG-20 sample has the highest cooling rate, whereas the G-5 sample shows the lowest. This suggests that increasing the WC content leads to an increase in cooling rate and a corresponding refinement in microstructure. The reduction in grain size with increasing WC content may be partially attributed to heterogeneous nucleation on WC particles, although this effect is inferred from composition differences and was not directly observed. The high thermal conductivity of WC helps with faster heat dissipation once the laser is turned off, thereby accelerating the cooling rate. It should be noted that the Hunt model primarily considers the metallic matrix solidification, and the presence of unmelted WC particles is not explicitly accounted for; thus, these values serve as a comparative estimation of relative cooling trends among the samples.

Previous studies have reported that grain morphology is governed by the temperature gradient (G) and solidification rate (R), where a high G/R ratio favors the formation of columnar structures. The condition for solidification stability can be expressed as follows [22]:

$$\frac{G}{R} \geq -\frac{m_l C_s^* (1 - k_0)}{k_0 D_l} \tag{2}$$

In this context, G and R represent the temperature gradient and solidification rate, respectively, while ml, C*, k0, and Dl denote the liquidus slope, solute concentration in the solid at the solid–liquid interface, partition coefficient, and diffusion coefficient in the liquid, respectively. In additive manufacturing processes, as the build progresses from the initial layers to the upper layers, the accumulation of heat within the part increases, leading to a greater instability of the solidification front. As a result, the microstructure gradually transitions from cellular to columnar dendrites and eventually to equiaxed dendrites. This phenomenon occurs because each deposited layer not only undergoes its melting and solidification but also contributes to the partial reheating of the underlying layers. With an increasing number of layers, the heat conduction path toward the substrate (which acts as a heat sink) becomes longer, making heat dissipation more difficult. Thus, the temperature gradient (G) decreases, and according to Equation 2, the stability of the solidification front is reduced.

Although adjusting laser parameters is one method for controlling the G/R ratio, in this study, due to the constant process parameters, changing the alloy composition—specifically increasing the tungsten carbide (WC) content—was adopted as an alternative strategy for controlling the microstructure. Increasing WC content increases the deviation from stable solidification conditions, thereby reducing the stability of the solidification front. However, microscopic analysis revealed that the vertical evolution of microstructure was not continuous; instead, it alternated periodically between different solidification modes (cellular and columnar dendritic). This periodicity is attributed to the layer-by-layer and discontinuous nature of the additive manufacturing process. Furthermore, as the build height increases, G decreases while R potentially increases due to reduced local cooling, resulting in a lower G × R value and thus favoring the growth of coarser dendrites.

However, in the composite samples, we observed that an increased volume fraction of tungsten carbide particles in the upper layers, due to their high thermal conductivity, enhanced the cooling rate and thus promoted the formation of finer-grained structures.

Table 4
Presents the average cooling rates of the composite clads, calculated based on the Hunt equation.

Sample	Value (K/s)
NG-20	7.77×10^6
G-5	2.6×10^6
G-10	3.05×10^6

To assess the influence of different compositional transition strategies between the substrate and the clad, EDS line scans were performed across the sample cross-sections. The results, presented in Fig. 8, reveal an intermixing zone at the interface between the stainless steel substrate and the IN718-based clad in all specimens. This intermixing zone, containing Ni, Fe, and Cr, results from material dilution during the cladding process and reflects elemental intermixing caused by melting, convection-driven mixing, and diffusion between the adjoining layers. In the NG-20 sample, which lacks a graded interlayer, the elemental transition occurs over a narrower region with a steeper gradient, resulting in a sharper and more distinct clad–substrate interface. In contrast, the G-5 and G-10 samples, which incorporate gradient cladding designs, exhibit more uniform and continuous elemental distributions across the interface. This indicates that the use of graded layers effectively reduces compositional discontinuity and enhances chemical compatibility. These findings underscore the capability of the L-PBF process in fabricating functionally graded clads with improved interfacial integrity.

Fig. 9 illustrates the characteristics of the reinforcing WC particles and the gradual transition layer formed at their interface with the IN718 matrix. The interface is visible at the boundary between the reinforcing particles and the matrix, indicating localized metallurgical interaction in this region. Linear EDS analysis results for the NG-20 sample show that approximately 71.39% tungsten and 22.58% carbon from the WC particles were detected at the interface (point 9 in Fig. 9a). Additionally, Ni, Cr, and Fe from the IN718 alloy were identified in this region with concentrations of 1.53% Ni, 3.16% Fe, and 1.18% Cr, respectively. These findings suggest that an interfacial reaction, specifically elemental interdiffusion and carbide formation, has taken place at the interface between the WC particles and the IN718 matrix, resulting in the formation of a gradual W_xC_y layer between these two phases. During this process, tungsten and carbon atoms are released due to surface decomposition of the WC particles and react with Ni, Cr, and Fe—the main alloying elements of IN718—forming new compounds at the interface. Due to the concentration gradient between the particles' surface and the matrix, atomic diffusion begins in this region. In this diffusion process, atoms migrate from one phase to another, strongly influenced by the concentration differences between the two phases. When atoms move from the WC phase into the IN718 matrix or vice versa, their movement is limited due to differences in chemical composition. In other words, atomic movement encounters resistance and barriers that slow down or even stop its migration along specific paths.

Throughout this process, tungsten and carbon atoms released from the WC particle surfaces diffuse toward the IN718 matrix, while Ni, Cr, and Fe atoms migrate in the opposite direction. As the diffusion path length increases, the mismatch in crystal structure and chemical composition between the WC particles and the IN718 matrix acts as a stronger diffusion barrier, thereby reducing the overall diffusion rate. Consequently, higher concentrations of tungsten and carbon are retained at the interface, whereas the concentrations of Ni, Cr, and Fe decrease due to their migration toward the particle surfaces..

In the region where diffusion occurs gradually (the diffusion zone), this trend reverses (point 10 in Fig. 9a), showing higher concentrations of Ni, Cr, and Fe and lower amounts of tungsten and carbon (with concentrations of 22.16% Ni, 21.69% Fe, 20.81% Cr, 26.86% W, and 8.39% C, respectively). This chemical diffusion process causes compositional changes at the interface and in the surrounding areas, reflecting the complex interaction resulting from the compositional and structural differences between the WC reinforcing particles and the IN718 matrix.

The formation of concentration gradients has also been reported in other studies, including the work by Rong et al. [15]. Fig. 10 illustrates the mechanism of interface formation and the diffusion layer between

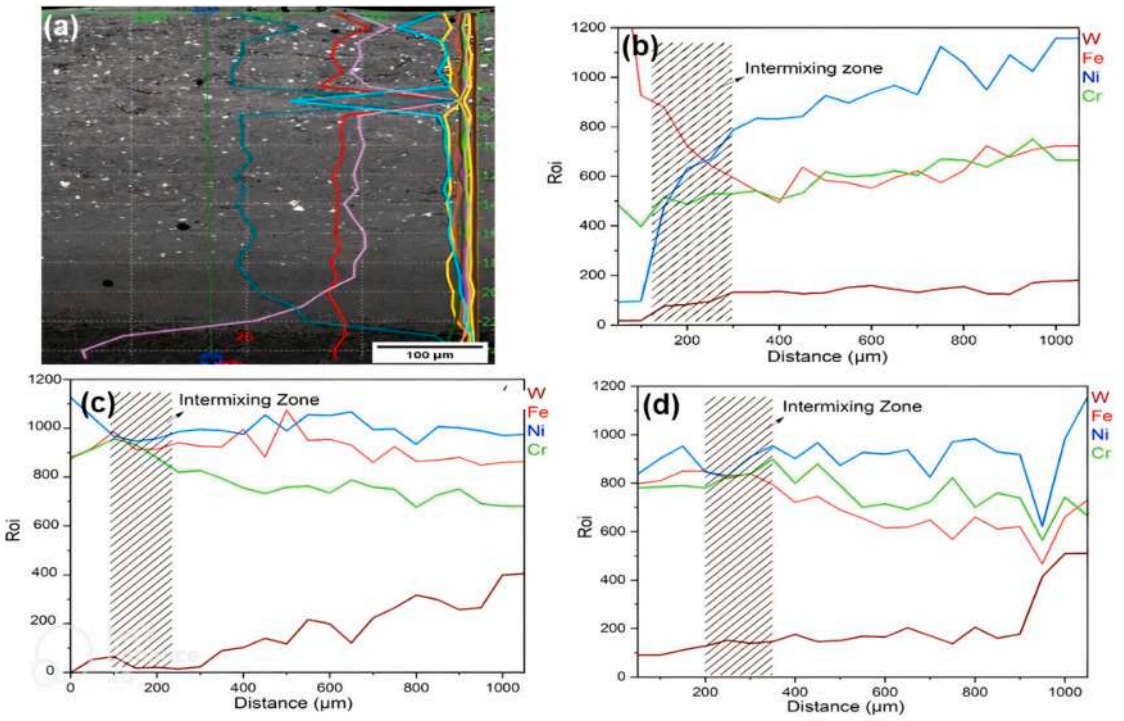

Fig. 8. SEM image and EDS line scan results across the cross-section: (a) Macroscopic cross-sectional image of the sample showing the selected path for the EDS line scan; (b–d) Elemental distribution profiles along the cross-section for samples NG-20, G-5, and G-10, respectively.

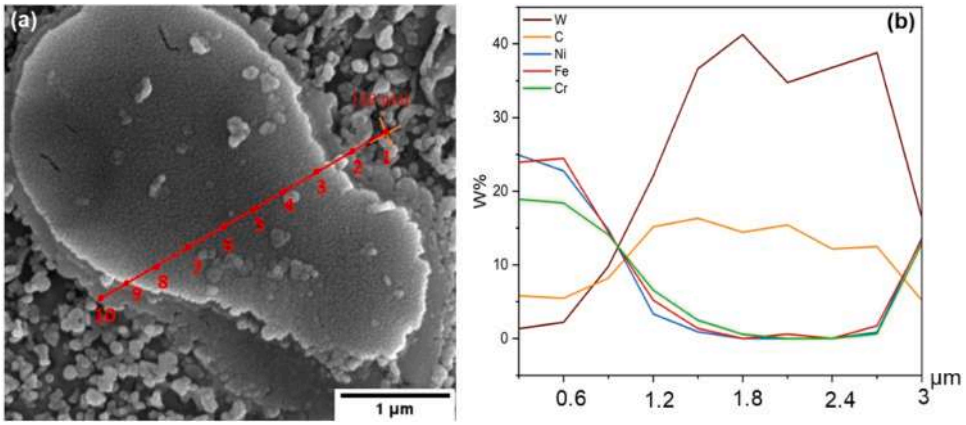

Fig. 9. SEM image and linear EDS analysis of a WC particle in the NG-20 sample. (a) Selected WC particle and linear scan path, (b) Elemental concentration profiles along the scan line.

the WC reinforcing particles and the IN718 matrix.

3.3. Hardness Test

In the Vickers hardness test, due to the dispersion of hard WC particles and reactive regions at the interface, it was sometimes unavoidable for the indentation to be placed near these areas. Since the indenter cannot easily penetrate the WC particles, their proximity caused the recorded local hardness values to be higher than the actual matrix hardness, leading to fluctuations in the data. To reduce this error, the final hardness value was calculated as the average of three nearby points. The results shown in Fig. 11 indicate that the hardness of the WC-reinforced claddings increased notably compared to the substrate and decreased continuously from the surface toward the substrate. This increase is attributed to the more uniform distribution of reinforcement particles due to the remelting of layers during the L-PBF process.

In the NG-20 sample, the highest hardness we observed near the surface was 439 HV; however, near the stainless steel substrate, hardness decreased in some regions due to local agglomeration of WC particles, leading to uneven particle distribution and stress concentration. In the G-5 sample, hardness increased gradually from the interface to the surface, reaching approximately 450 HV in the final clad layer (20% WC). This gradual compositional change can disrupt solidification, leading to coarser grain growth and an uneven distribution of WC. The G-10 sample has the highest hardness in the fourth layer (480 HV), which is attributed to the gradient design, uniform WC distribution, reduced porosity, and improved bonding between layers. This gradient distribution also resulted in a more uniform stress distribution and a stronger microstructure. The positive effect of microstructural gradation on hardness improvement has also been confirmed in the study by Wang et al.[26].

Regarding the SS17-4PH substrate, its hardness (252HV) is slightly

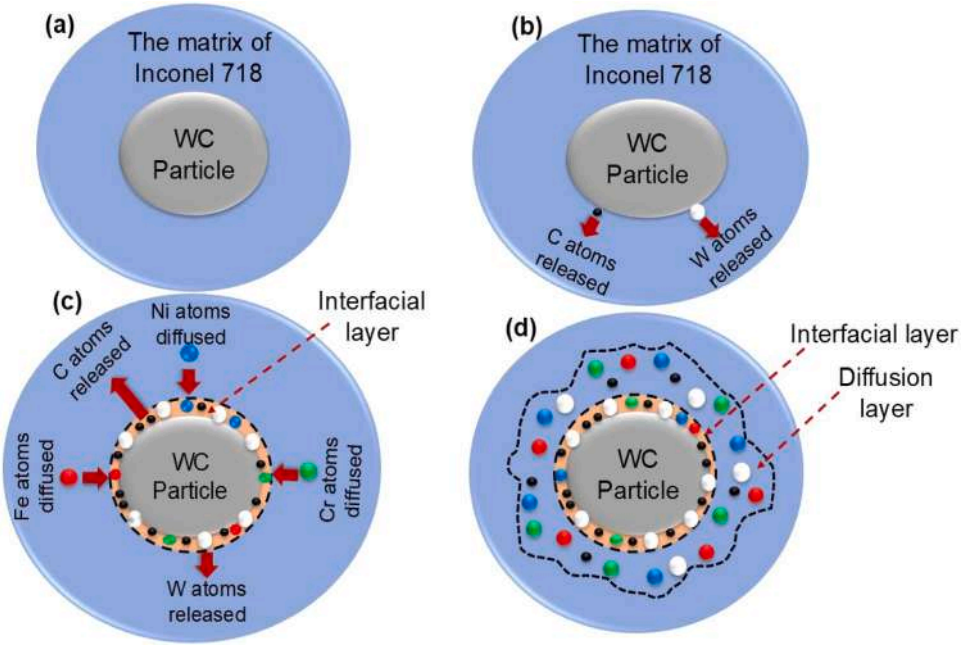

Fig. 10. Schematic of the mechanism for the formation of the interface and diffusion layer between WC particles and the IN718 matrix. a) View of the IN718+WC composite, b) Local decomposition of WC and release of C and W elements, c) Migration of Fe, Ni, and Cr elements from the matrix toward WC particles, and d) Formation of the diffusion layer in the boundary region between WC and the matrix.

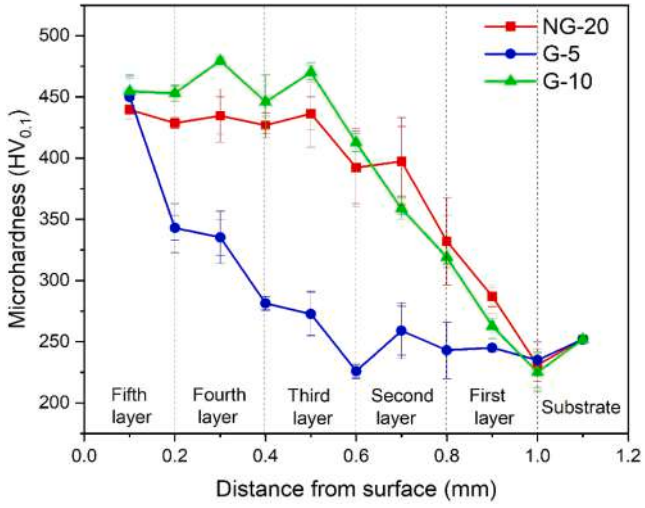

Fig. 11. Microhardness profiles across the cross-sections of NG-20, G-5, and G-10 composite clads, from the substrate to the top layer. Each data point represents the average of three measurements at the same height.

lower than that of the forged condition, which is attributed to the absence of heat treatment (such as aging) in the SLM-fabricated samples. Additionally, the presence of austenite in the samples could be another reason for the lower hardness, although this phase contributes to toughness and strength. Similar behavior has been reported in the study by Garcia-Cabson et al. [27].

3.4. Wear Test

3.4.1. Wear Rate Results

The wear rate ($mm^3/N{\cdot}m$) was calculated using the Archard equation for the substrate and the composite claddings [28]:

$$K = \frac{V}{F_n.L} \tag{3}$$

Where V is the volume loss in mm^3, F_n is the applied load in newtons, and L is the sliding distance in meters.

The wear rate results obtained at room temperature and 350°C are presented in Fig. 12. A comparison of the wear graphs at room temperature (Fig. 12a) reveals differences in wear resistance. As observed, the wear rate of the 17-4PH stainless steel substrate is 3.905×10^{-4} $mm^3/N{\cdot}m$, which is higher than all the composite claddings. This indicates that the application of the cladding notably enhances the wear resistance of the substrate. Among the claddings, the non- graded sample (NG-20) has the highest wear rate of 3.381×10^{-4} $mm^3/N{\cdot}m$, followed by the graded sample G-10 with a wear rate of 3.155×10^{-4} $mm^3/N{\cdot}m$, and finally, the graded sample G-5 shows the lowest wear rate of 2.424×10^{-4} $mm^3/N{\cdot}m$.

Fig. 12b shows the wear rate results of the test performed at 350°C. Overall, the wear rate decreased at this higher temperature, which can be attributed to the formation of protective oxide layers at high temperatures. These oxide layers act as barriers against direct contact between the pin and the surface, functioning as solid lubricants and thereby improving wear resistance. This behavior has also been reported in previous studies, including the work by Varga et al. [29]. On high-temperature wear mechanisms. Consistent with the room temperature results, the highest wear rate at 350°C—1.6×10^{-5} $mm^3/N{\cdot}m$—was recorded for the 17-4PH stainless steel substrate. This further confirms that the application of composite cladding improves the wear resistance of the substrate even under higher temperature conditions. Among the clad samples, the non-graded NG-20 has the highest wear rate (1.2×10^{-5} $mm^3/N{\cdot}m$), followed by the graded sample G-10 (1.1×10^{-5} $mm^3/N{\cdot}m$), and finally, the G-5 sample with the lowest wear rate of 0.975×10^{-5} $mm^3/N{\cdot}m$.

The differences in wear performance among the claddings can be attributed to three main factors: hardness, matrix microstructure, and WC particle distribution. A uniform distribution of tungsten carbide particles within the IN718 matrix leads to increased hardness, reduced localized plastic deformation, and enhanced wear resistance. However, at higher volume fractions, these particles may act as abrasives themselves, causing surface scratching. The graded G-5 sample demonstrated the highest wear resistance due to its controlled WC content (5 wt%), which, together with the more uniform distribution of reinforcing

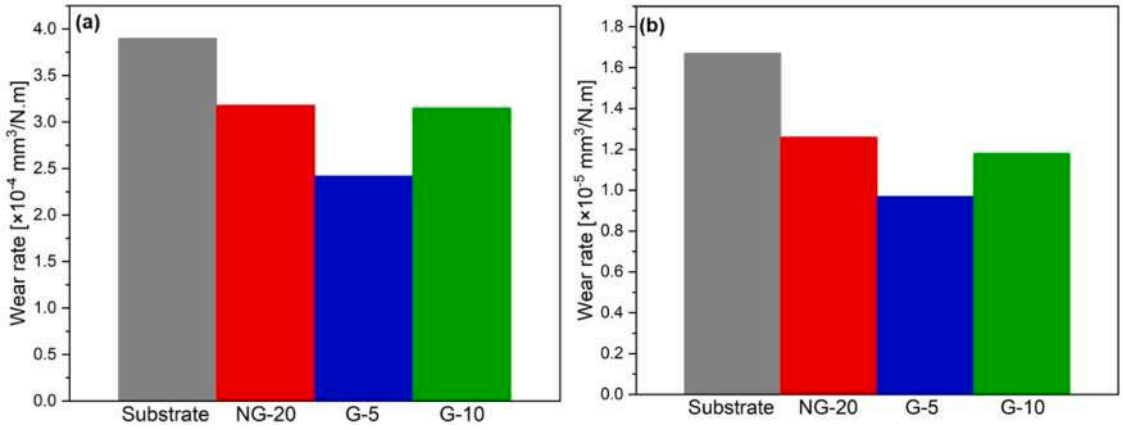

Fig. 12. Wear rate results for the 17-4PH substrate and IN718/WC composite clads at two temperatures: (a) room temperature and (b) 350 °C. Wear rate was calculated based on the volume loss of the samples over a 4-hour sliding test.

particles, denser microstructure, and smoother compositional gradient, resulted in reduced stress concentration and improved mechanical compatibility between layers.

Moreover, the gradient structure in G-5 allows for a gradual load transfer between the surface and subsurface layers, reducing local stress peaks and limiting direct abrasive interaction between the pin and hard particles. This effect is particularly significant at elevated temperatures, where the softer substrate would otherwise promote increased pin wear. Although the oxide layer formed on the surface of G-5 at higher temperatures is discontinuous and unstable, its rugged and mechanically robust subsurface structure effectively resists further mechanical degradation, thereby enhancing the overall wear resistance of the G-5 sample compared to NG-20 and G-10

3.4.2. *Friction coefficient results*

Fig. 13 shows that in all 17-4PH stainless steel samples with composite claddings, the coefficient of Friction (COF) initially exhibits an unstable wear stage with notable fluctuations (Zone I), which quickly transitions to a more stable wear stage (Zone II) characterized by reduced fluctuations. In this stable stage, the COF reaches a relatively constant value, attributed to the stabilization of the contact surface and more consistent wear conditions. This two-stage wear behavior is consistent with the findings of Xie et al.[30], It is related to the initial engagement of surface asperities and the gradual increase in the effective contact area. Over time, the accumulation of wear debris complicates the contact interface between the pin and the surface, and fluctuations in the COF are mainly due to instantaneous changes in frictional resistance. Overall, the initially high COF values are caused by the roughness of the as-fabricated surface, which gradually decreases as the contact stabilizes. As shown in Fig. 13a, the application of composite claddings generally reduces the COF compared to the bare 17-4PH stainless steel substrate at room temperature. Fig. 13b presents the COF variations for the different samples at 350°C. A sharp drop in COF is observed during the first approximately 30 minutes of testing, attributed to the formation of oxide layers on the surface at higher temperatures. These oxide films act as solid lubricants, reducing direct metal-to-metal contact and thus lowering surface friction.

Table 5 reports the average coefficient of friction (COF) and wear rates for all samples at both temperatures. The average COF was calculated by taking the arithmetic mean of all recorded instantaneous COF values throughout the stable wear stage. At 350°C, an increase in COF was accompanied by a decrease in wear rate for the composite claddings, whereas at room temperature, a higher COF correlated with increased wear. This indicates that a higher coefficient of Friction does not necessarily correspond to higher wear. Note that COF and wear resistance are two independent properties influenced by factors such as wear mechanisms, contact conditions, and material properties. In some cases, high COF may coexist with good wear resistance, but this relationship is not universal.

3.4.3. *Wear Mechanism*

The wear mechanisms were examined at room temperature using

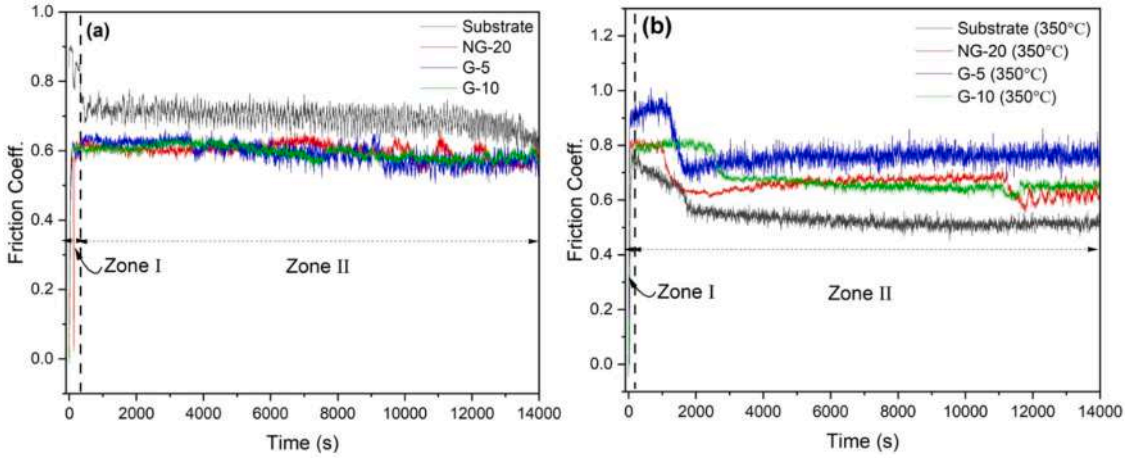

Fig. 13. Graphs of the friction coefficient (COF) versus time for the 17-4PH substrate and IN718/WC composite clads: (a) room temperature and (b) 350 °C. Measurement noise in the data has been filtered for clarity.

Table 5
Comparison of Coefficient of Friction (COF) and Wear Rate at Room Temperature and 350°C.

Temperature (°C)	Sample	Average Coefficient of Friction	Wear Rate ($mm^3/N{\cdot}m$)
Room Temperature	Substrate	0.6873 ± 0.0009	3.905×10^{-4}
	NG-20	0.5951 ± 0.0005	3.183×10^{-4}
	G-5	0.5919 ± 0.0007	2.424×10^{-4}
	G-10	0.5946 ± 0.0004	3.155×10^{-4}
350 °C	Substrate	0.5404 ± 0.0008	1.675×10^{-5}
	NG-20	0.6628 ± 0.0005	1.262×10^{-5}
	G-5	0.771 ± 0.001	0.975×10^{-5}
	G-10	0.6851 ± 0.0006	1.176×10^{-5}

SEM images presented in Fig. 14, which show the wear tracks of the 17-4PH substrate and the composite claddings. In the substrate (Fig. 14a), evidence of plastic deformation caused by localized high stresses at the pin–surface contact is observed, leading to irreversible surface layer deformation. Deep abrasive grooves produced by the mechanical action of the counterface and adhered wear debris resulting from localized bonding and detachment events are also visible, indicating the coexistence of abrasive and adhesive wear mechanisms. Furthermore, subsurface delamination associated with crack propagation, together with signs of mild oxidation, suggest that multiple damage mechanisms simultaneously contribute to the overall wear behavior of the substrate.

In the NG-20 clad (Fig. 14b), the alignment of hard WC particles in the sliding direction suggests that abrasive wear is the dominant mechanism. These particles, due to their high hardness, penetrate into the contact surface and form deep grooves, clearly indicating the prevalence of abrasive wear. This type of wear originates from the direct and repeated interaction of hard particles with the clad surface, leading to distinct scratches and grooves along the wear path. At the same time, evidence of adhesive wear and microfractures is also visible. Localized contacts between the clad and the counterface promote adhesive bonding, followed by the detachment of surface fragments. Signs of cracking, delamination, and spalling are present on the worn surface, which can be interpreted as consequences of adhesive wear and the progression of surface cracks. This concept is illustrated in Fig. 15a, which presents the abrasive wear mechanism.

In the gradient-clad G-5 (Fig. 14c), the reduction in groove depth indicates higher wear resistance compared to the other samples. The irregular distribution of WC particles decreases stress concentration and leads to adhesive wear being the dominant mechanism, manifested as material delamination and the release of flake-like debris. These damages, together with mild oxidation, can be explained by the schematic representation of the adhesive wear mechanism shown in Fig. 15b. A key difference between the G-5 and NG-20 clads lies in the orientation and distribution of tungsten carbide particles on the surface. In the G-5 sample, the hard particles are not aligned along the sliding direction, which reduces stress concentration and consequently lowers the severity of abrasive wear. This behavior can be explained by a more uniform distribution of hard particles and better stress accommodation in the gradient structure, which reduces localized pin–clad interactions and mitigates severe pin wear. As a result, the surface of this clad is mainly governed by adhesive wear. In this case, the formation and propagation of cracks induced by shear stresses and localized plastic deformation cause layer-by-layer material removal, releasing flake-shaped wear debris. Moreover, localized forces between abrasive particles and the surface promote the detachment of certain regions of the clad, leading to discontinuous and localized surface damage. Although signs of mild oxidation are also detected, its contribution is negligible compared to abrasive and adhesive wear, and it is regarded only as a secondary phenomenon. An important observation in this sample is that despite the improved wear resistance of the clad, the pin experienced noticeable wear, which may be attributed to more active interaction between the pin surface and abrasive particles or to the relatively lower hardness of some regions of the clad surface.

In the G-10 clad (Fig. 14d), similar to NG-20, the alignment of hard WC particles along the sliding direction results in deep grooves and the dominance of abrasive wear. In addition to abrasive wear, minor signs of adhesive wear are also observed, along with slight oxidation in some areas, likely caused by localized temperature rise due to friction; however, its contribution to the overall wear process is relatively insignificant. Notably, the pin in this sample experienced less wear compared to the G-5 clad. This behavior may be attributed to a more favorable distribution of hard particles or a more stable contact surface in the G-10 clad, which reduces the occurrence of pin-to-clad counter wear.

Fig. 16 presents the EDS analysis results from the wear track of the IN718/WC composite. Region 1 shows a high concentration of tungsten, indicating the detachment of WC particles from the surface due to mechanical stresses and their involvement in the abrasive wear mechanism. Region 2 also contains a notable amount of carbon, which may result from the decomposition of tungsten carbide. This value is interpreted as evidence of adhesive wear and material transfer between the contacting surfaces. The presence of a small amount of oxygen in both regions suggests the formation of a thin oxide layer during the wear process, which can temporarily enhance wear resistance by reducing direct contact between the ball and the coating surface. However, with increased sliding distance and repeated mechanical stress, this oxide layer becomes cracked and eventually fails. Overall, a combination of abrasive and adhesive wear mechanisms, along with the limited yet beneficial role of tribo-oxidation, can be identified in the wear behavior of this composite.

Fig. 17 shows SEM images of the wear tracks on the substrate and composite claddings at elevated temperatures. In the substrate (Fig. 17a), oxidative wear dominates, manifested by the formation of brittle oxide layers that constitute the main wear products. Additionally, adhesive wear is evident in the form of delamination in certain areas, resulting from high adhesive forces between contacting surfaces that cause portions of the substrate surface to detach during sliding. Shallow grooves are also observed in some regions, indicating the contribution of abrasive wear, which may originate from hard particles or oxide debris trapped between the contacting surfaces.

In the NG-20 cladding (Fig. 17b), a relatively thick and continuous oxide layer covers the surface, indicating the dominance of oxidative wear. The formation of this layer can reduce metal-to-metal contact and consequently lower the friction coefficient. Although slight evidence of adhesive wear is observed, abrasive wear plays an almost negligible role. Limited delamination is also detected in some regions, which may reflect mild adhesive wear, likely resulting from localized bonding between the substrate surface and the counterface, followed by the restricted detachment of surface layers.

In the gradient G-5 cladding (Fig. 17c), multiple wear mechanisms, including oxidative, adhesive, and abrasive wear, were simultaneously observed. Discontinuous oxide layers, surface cracks, and distinct grooves were generated due to stress concentration and the spallation of hard or oxidized particles. This behavior can be explained by the gradient structure and more stable subsurface, which reduces severe localized pin–clad interactions, leading to enhanced wear resistance. Although the surface of NG-20 appeared more stable, its wear rate was higher, likely as a result of oxidation and subsurface degradation—this behavior was also reported by Mao et al.[31]. In contrast, the G-5 cladding exhibited higher wear resistance owing to its gradient structure and more stable subsurface.

In the G-10 sample (Fig. 17d), oxidation was more pronounced than in G-5, likely due to the different distribution of WC particles and the thermal characteristics of the surface. In addition, signs of adhesive and abrasive wear, manifested as delamination and shallow grooves, were observed, indicating the simultaneous operation of multiple wear mechanisms in this sample.

According to the elemental distribution maps of the composite

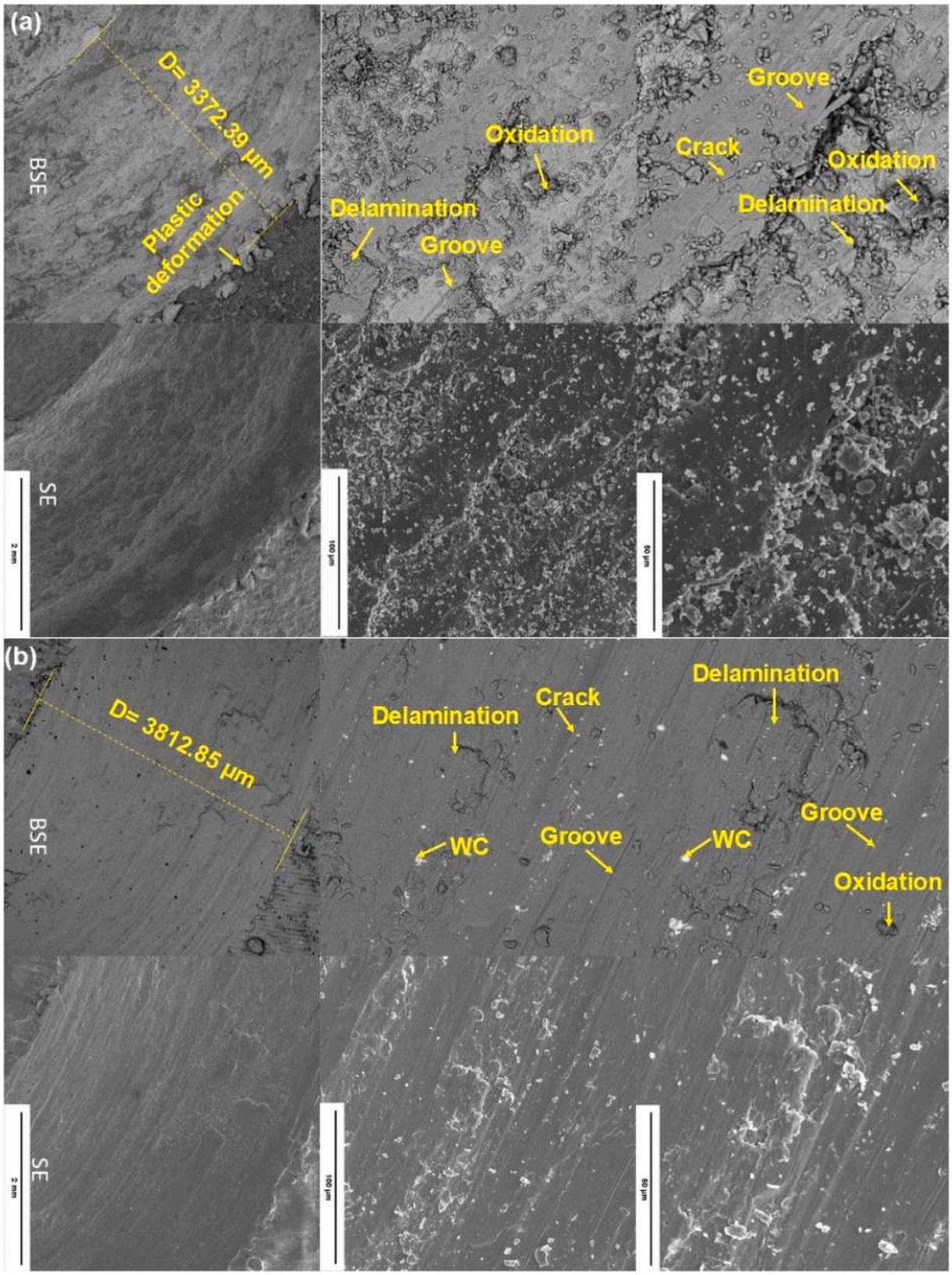

Fig. 14. SEM images of wear tracks at room temperature: (a) 17-4PH substrate; (b–d) NG-20, G-5, and G-10 composite claddings, respectively. Each sample is shown at three magnifications to highlight differences in wear mechanisms, local WC particle distribution, and the influence of compositional grading on wear behavior.

cladding (Fig. 18) at 350°C, oxygen (O) was detected on the worn surface. This oxygen reacted with iron (Fe) from the IN718 superalloy matrix and the steel pin, forming iron oxides. Moreover, the presence of chromium (Cr) and nickel (Ni) suggests the possible formation of more

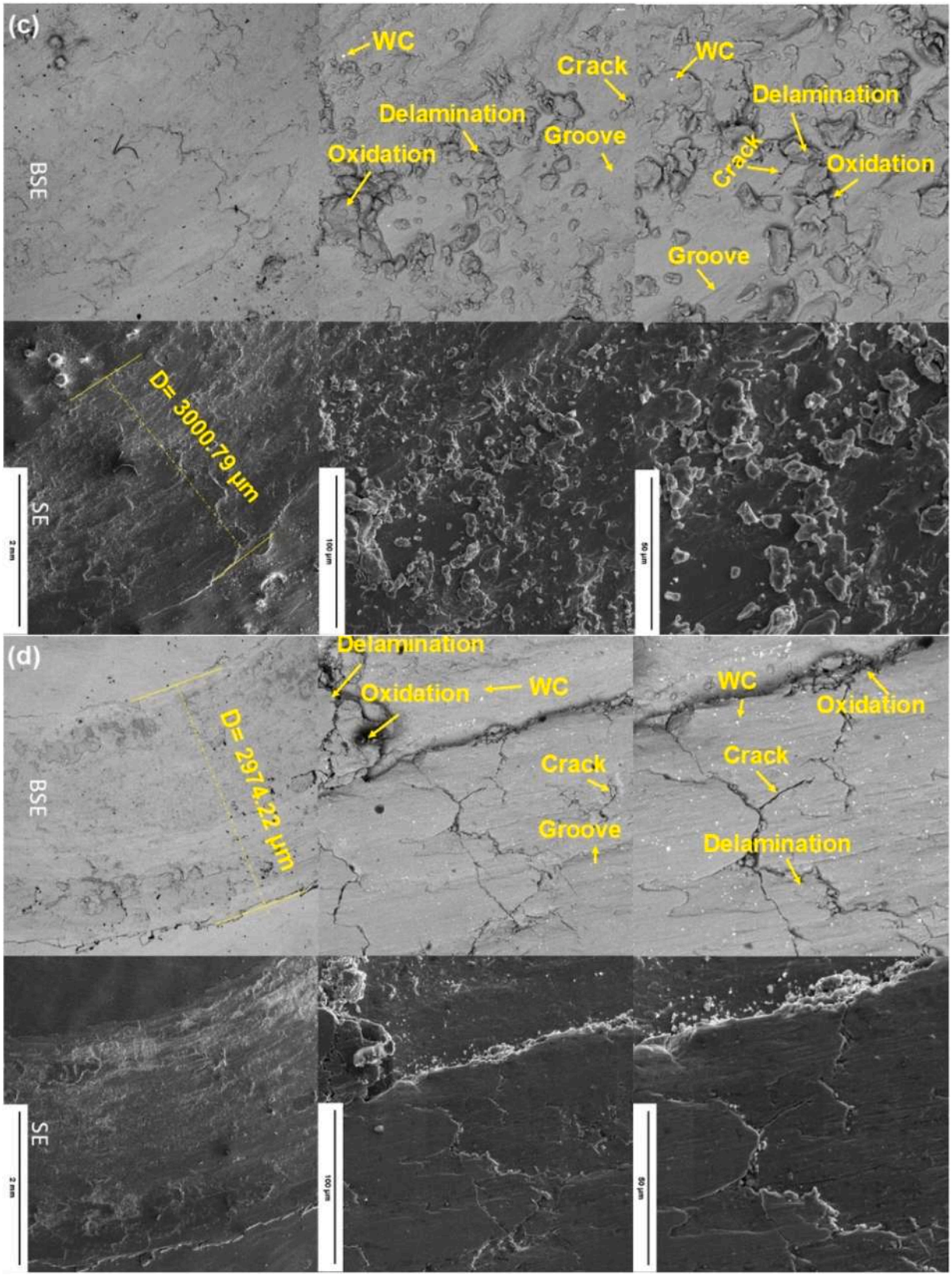

Fig. 14. (*continued*).

complex oxides, such as chromium-iron and nickel-iron oxides. The tungsten carbide (WC) particles, acting as the challenging phase, mainly remained stable within the structure. The gradient distribution and more uniform arrangement of hard particles in the G-5 cladding reduce stress concentration and mitigate direct severe interactions between the softened pin and hard particles, improving wear resistance at elevated temperatures.

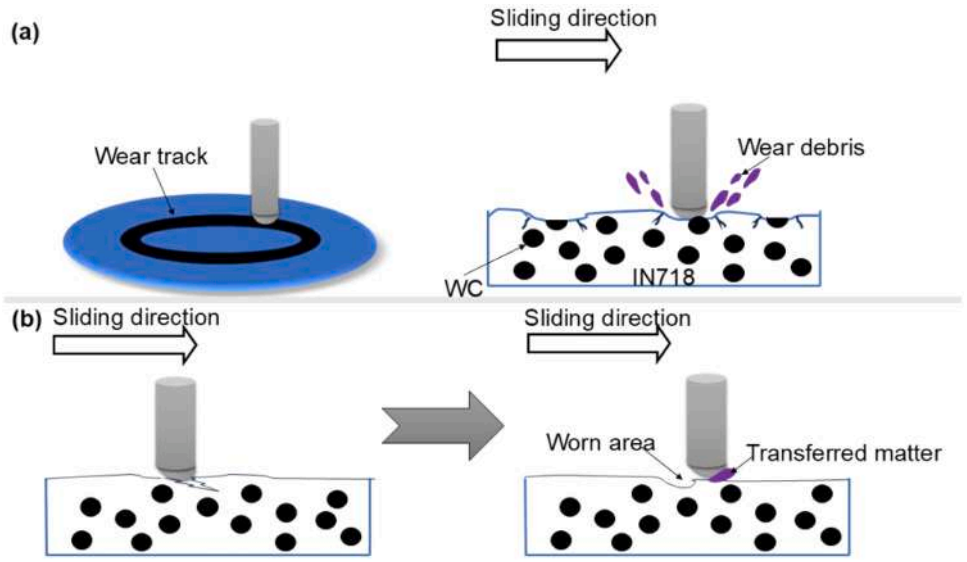

Fig. 15. Schematic of wear mechanisms: (a) Abrasive wear, and (b) Adhesive wear.

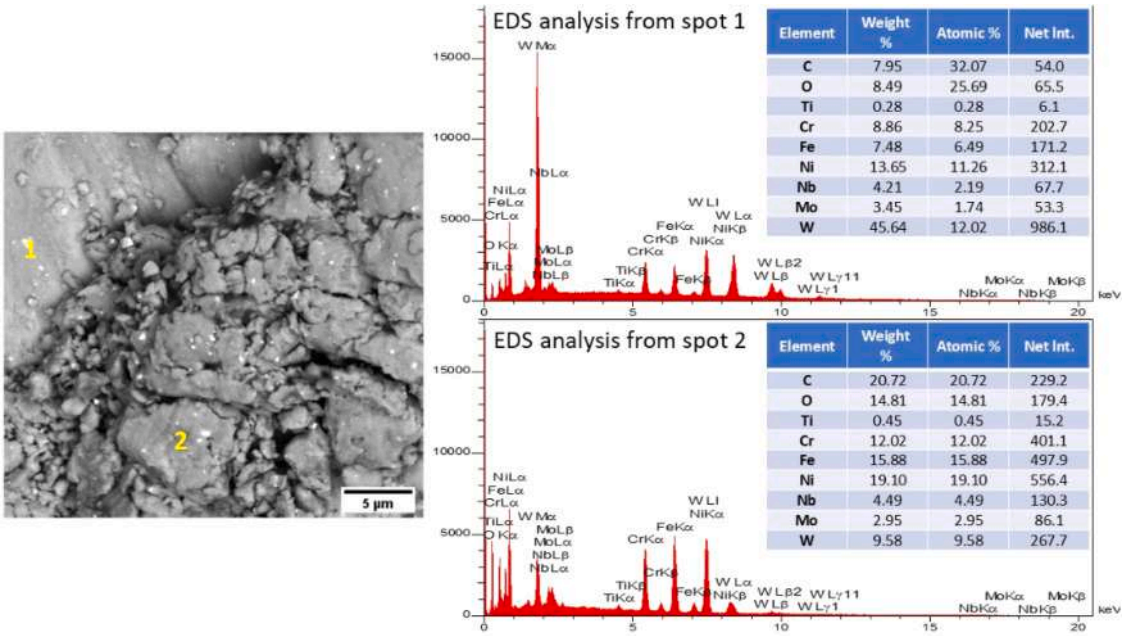

Fig. 16. EDS analysis of wear tracks on the IN718/WC composite cladding at regions 1 and 2, highlighting the presence of mild oxidation in region 2 at room temperature.

3.4.4. Pin Height Reduction in Pin-on-Disk Wear Tests

In pin-on-disk wear tests, one of the key parameters for accurately analyzing the wear behavior of samples is the measurement of pin height reduction after testing, which was performed directly using a digital caliper to ensure accurate and reliable evaluation. Along with the wear rate and average coefficient of friction (COF), this parameter provides valuable information regarding contact type, surface engagement intensity, relative hardness, and wear resistance. As shown in Fig. 19, at room temperature, the greatest pin height reduction was observed for the gradient G-5 sample, measuring 0.09 mm. This behavior can be attributed to the high surface hardness of this sample and the uniform distribution of hard WC particles in the surface layer. Under these conditions, although the sample surface exhibited high wear resistance, the increased mechanical interaction with the pin resulted in higher wear on the pin itself. It should be noted that in gradient claddings, the gradual transition in hardness and elastic modulus reduces stress concentration at the contact interface, leading to a more stable load transfer during sliding. The G-10 sample showed a similar trend but with lower intensity, recording a pin height reduction of 0.07 mm. In contrast, the NG-20 sample, which lacks a gradient structure and has a uniform composite layer, produced milder mechanical contact, with a pin height reduction of 0.05 mm. In this case, part of the frictional energy was consumed in surface layer wear, resulting in comparatively lower pin wear. Finally, the smallest pin height reduction was observed in the 17-4PH steel substrate, measuring 0.03 mm. This can be attributed to the lower hardness of the substrate, which led to the majority of wear occurring on the sample surface, thereby minimizing pin wear.

In examining the frictional and wear behavior of the claddings and the steel substrate at 350 °C, it was observed that softening of the metallic substrate (IN718) and the reduced mechanical resistance of the

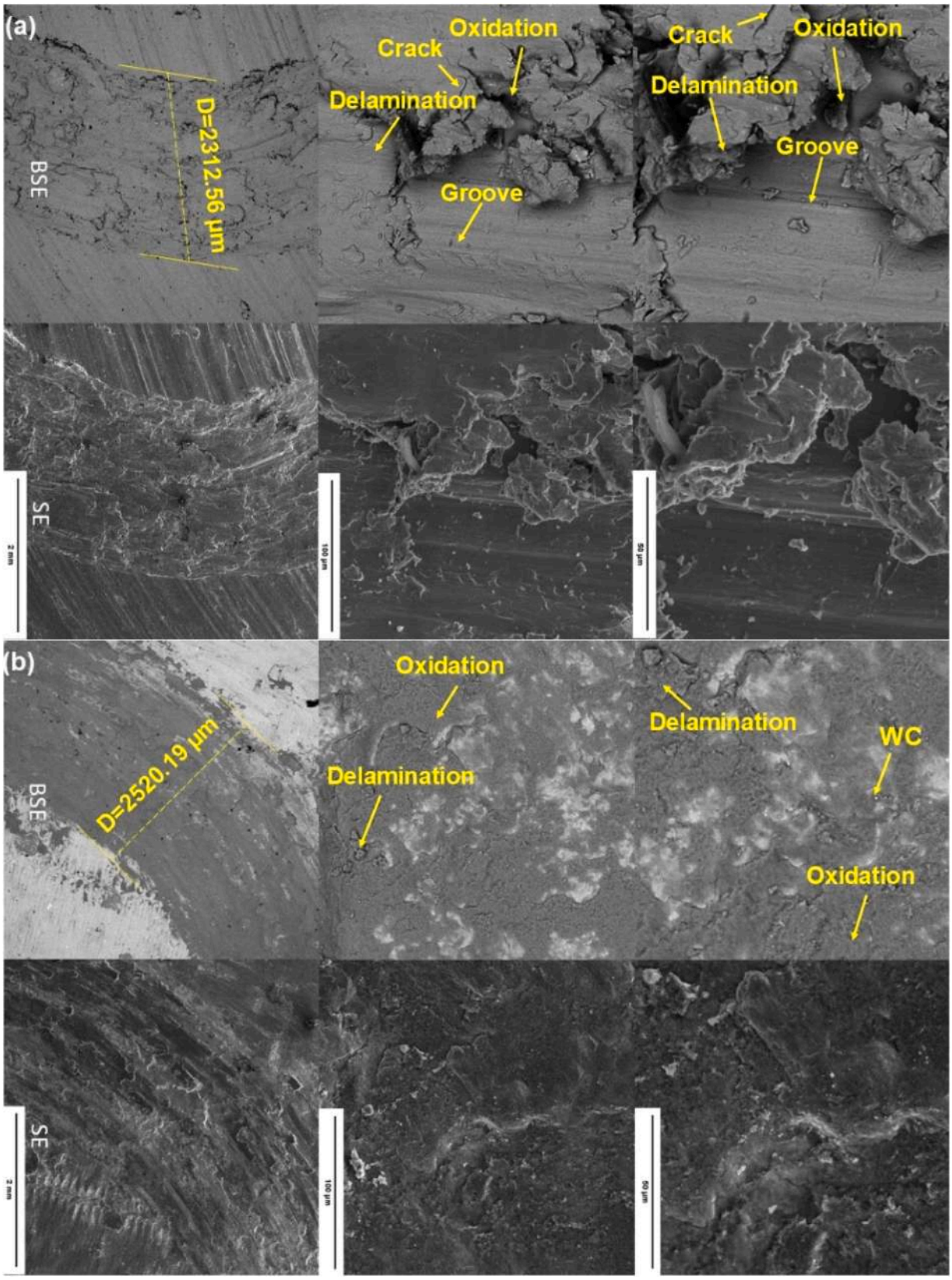

Fig. 17. Graphs of the friction coefficient (COF) versus time for the 17-4PH substrate and IN718/WC composite clads: (a) room temperature and (b) 350 °C. Measurement noise in the data has been filtered for clarity.

steel pin amplified the role of hard particles in the contact, resulting in increased pin wear. Among the claddings, the G-5 sample exhibited the lowest pin height reduction (0.53 mm) despite a higher coefficient of friction, which is attributed to its gradient structure and uniform stress

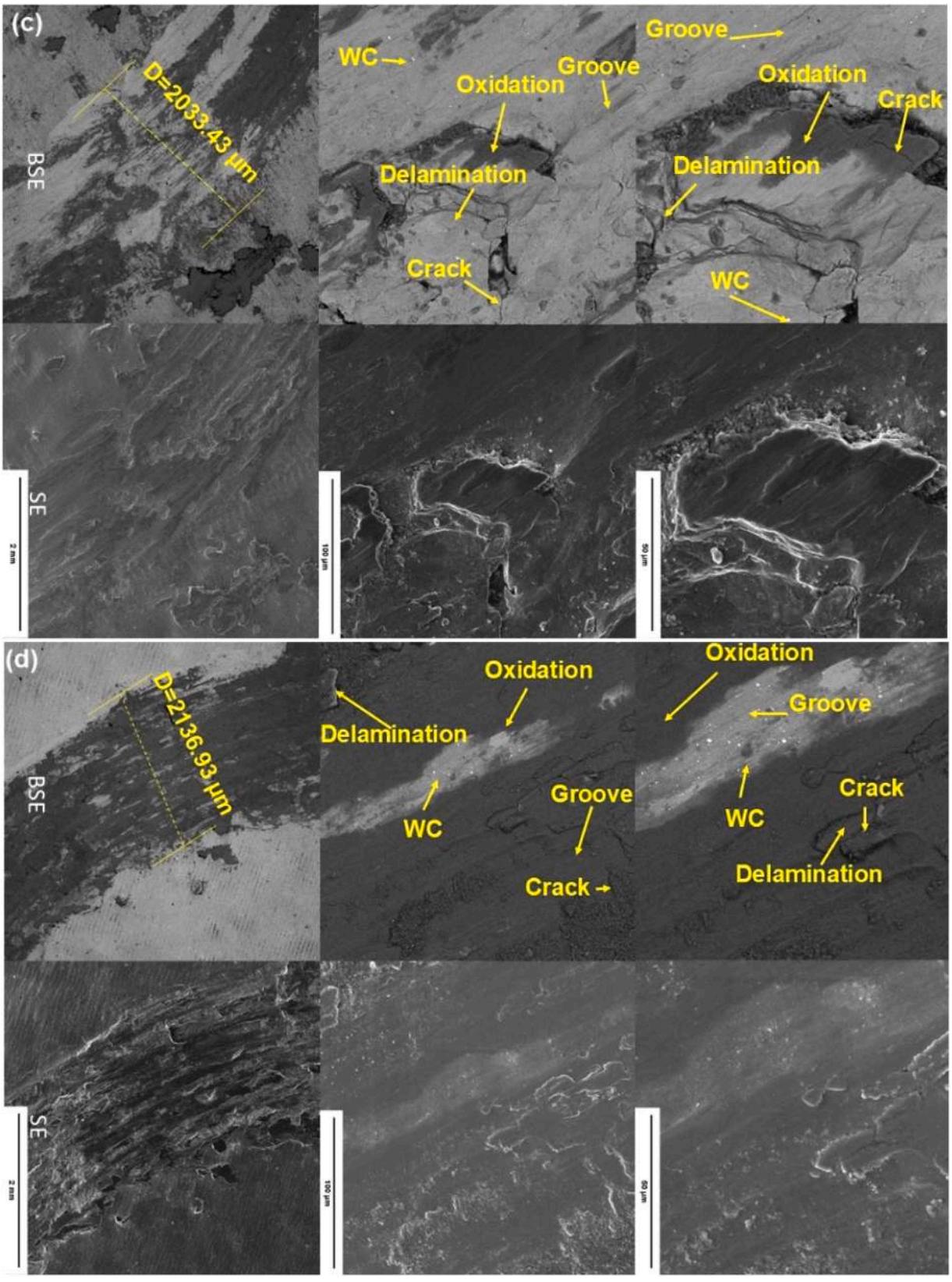

Fig. 17. (*continued*).

distribution on the surface. This behavior is associated with the graded structure, which promotes a more uniform subsurface stress distribution and mitigates direct, localized interaction between the softened pin and hard particles. In contrast, the NG-20 sample, with a lower coefficient of friction, experienced the highest pin wear (0.63 mm) due to direct contact between the softened pin and hard particles and the absence of a gradient structure in the clad. Under the same conditions, the 17-4PH steel substrate showed the lowest pin wear (0.36 mm), which can be

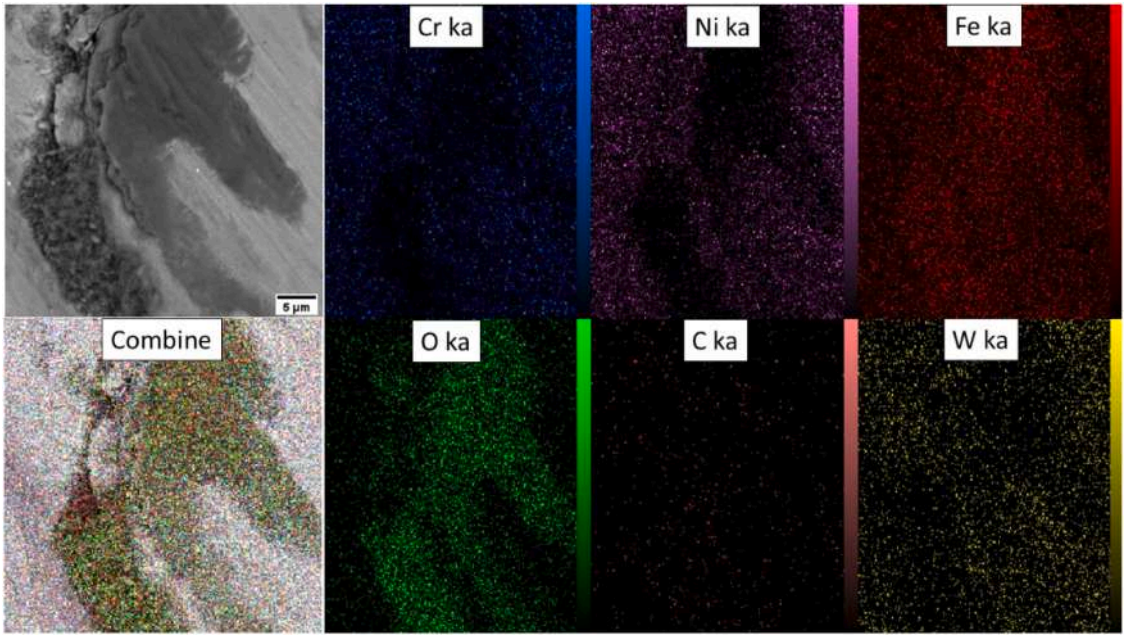

Fig. 18. Elemental distribution maps of the wear track at 350 °C, highlighting severe oxidation along the worn surface.

attributed to the formation of lubricating oxide layers on the sample surface and, simultaneously, the significant reduction in substrate hardness at elevated temperatures. This behavior allowed frictional energy to be absorbed and prevented direct, damaging contact between the pin and hard particles. It is noteworthy that at room temperature, the trend was reversed, with the G-5 sample, despite its higher surface hardness, showing the highest pin wear. This contrast indicates that at low temperatures, surface hardness and physical roughness predominantly govern wear, whereas at elevated temperatures, thermo-mechanical stability, pin softening, and the formation of protective surface layers primarily determine the frictional and wear behavior of the system.

5. Conclusion

In the present study, the integrated additive manufacturing of a graded composite IN718/WC coating on a 17-4PH martensitic stainless steel substrate using L-PBF was examined from metallurgical and mechanical perspectives. The main findings are summarized as follows:

1 All samples were fabricated to a high standard, showing no visible cracks, delamination, or discontinuities. The graded sample G-5 exhibited the lowest porosity (0.32%) and demonstrated a more uniform microstructure compared to the other samples.
2 XRD analysis revealed that the microstructure of the 17-4PH substrate consisted mainly of martensite (72%) with retained austenite (28%). In the IN718/WC coatings, γ-phase, WC, and Laves phases were identified.
3 Microstructural observations revealed that increasing the WC content resulted in a larger melt pool, higher cooling rates, and the formation of finer grains. The NG-20 sample, which contains the highest WC content, exhibits the fastest cooling rate and the smallest dendrite arm spacing.
4 Elemental distribution analysis revealed a more uniform chemical composition in the graded samples, characterized by a smoother transition zone compared to the non-graded sample. Furthermore, at the interface between WC particles and the IN718 matrix, a WxCy diffusion layer with a gradual composition was observed, resulting from the exchange of W and C with Ni, Cr, and Fe elements.
5 The graded design improved both hardness and microstructural uniformity. Sample G-10 has the highest hardness (480 HV), representing a 91% increase compared to the substrate, while G-5 also demonstrated notable performance with a hardness of 450 HV (79% increase), effectively preventing localized particle agglomeration.
6 Wear tests conducted at room temperature showed that all coatings outperformed the substrate. Sample G-5, with a friction coefficient of 0.591 and a wear rate of 2.424×10^{-4} $mm^3/N{\cdot}m$, delivered reasonable performance, reducing the wear rate by 38% compared to the substrate. Samples G-10 and NG-20 showed reductions of 19% and 18%, respectively. At 350°C, wear performance further improved, with G-5 having a friction coefficient of 0.771 and a wear rate of 0.975×10^{-5} $mm^3/N{\cdot}m$, achieving a 42% reduction in wear rate compared to the substrate and outperforming other samples. These results highlight that a higher friction coefficient does not necessarily imply better wear resistance; G-5 demonstrated the highest wear resistance despite its relatively higher friction coefficient.
7 SEM analysis of the wear tracks at room temperature revealed severe abrasive and adhesive wear on the substrate, while in G-5, wear was mainly adhesive, characterized by surface cracks and delamination. At 350°C, oxidation was the dominant wear mechanism in all samples, accompanied by minor adhesive and abrasive wear features.

Considering its combination of low porosity, relatively uniform WC particle distribution, 79% hardness increase relative to the substrate, and superior wear performance at both room temperature and 350 °C, sample G-5 was identified as the most suitable candidate among the investigated gradient designs. These findings suggest that a graded design with a gentler gradient step, such as G-5, can provide reliable mechanical and wear performance for industrial applications, including the oil, gas, and petrochemical sectors. It should be noted, however, that finer gradient steps or different layer configurations could potentially further improve performance, which remains a topic for future investigation. Additionally, the LPBF process's capability to fabricate complex, graded coatings enables the optimization of functional properties, making it a practical option for advanced engineering applications.

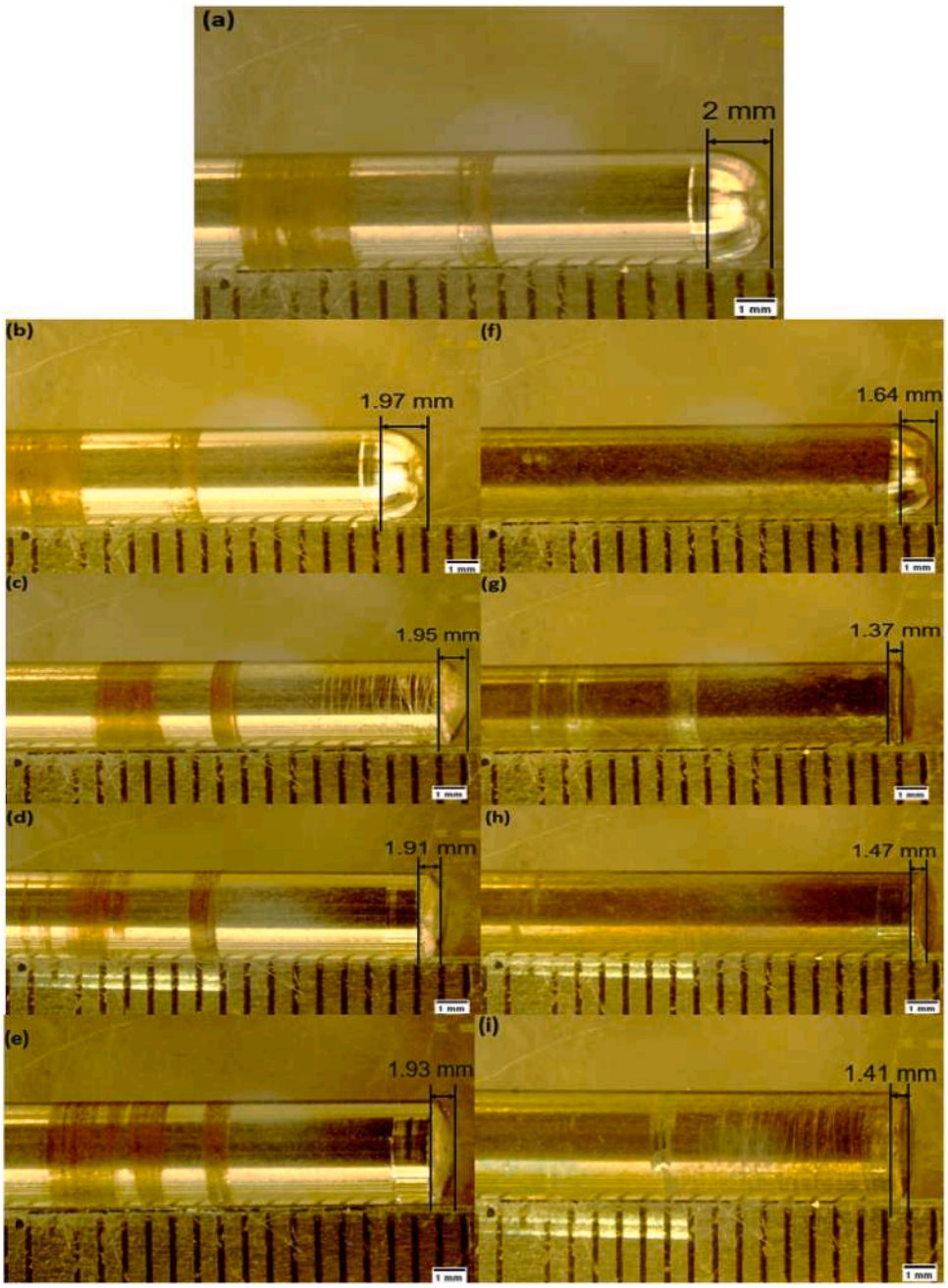

Fig. 19. Stereo microscope images of the AISI 52100 steel pins. (a) Before the wear test, (b–e) worn pins at room temperature after the wear test for the substrate, NG-20, G-5, and G-10 samples, respectively; (f–i) worn pins at 350 °C after the wear test for the substrate, NG-20, G-5, and G-10 samples, respectively.

Data availability statements

All data generated or analyzed during this study are included in this article.

CRediT authorship contribution statement

Hadise Imani: Writing – original draft, Investigation. **Homam Naffakh-Moosavy:** Writing – review & editing, Supervision, Conceptualization. **Mohammad Taghian:** Writing – review & editing. **Abdollah Saboori:** Writing – review & editing, Resources, Methodology. **Luca Iuliano:** Writing – review & editing.

Declaration of competing interest

The authors declare that they have no known competing financial interests or personal relationships that could have appeared to influence the work reported in this paper.

References

[1] Z. Lyu, Y.S. Sato, S. Li, W. Xu, Z. Xu, X. Hu, Q. Zhu, Tailoring microstructure and mechanical properties of 17-4PH steel fabricated by wire-arc directed energy deposition via a combination of intrinsic and post-processing heat treatments, Addit. Manuf. 80 (2024) 103954, https://doi.org/10.1016/j.addma.2023.103954.
[2] M. Merlin, C. Morales, M. Ferroni, A. Fortini, C. Soffritti, Influence of heat treatment parameters on the microstructure of 17-4 PH single tracks fabricated by direct energy deposition, Appl. Sci. 14 (2024) 20700, https://doi.org/10.3390/app14020700.

[3] G. Brando, F.R. Andreacola, I. Capasso, D. Forni, E. Cadoni, Strain-rate response of 3D printed 17-4PH stainless steel manufactured via selective laser melting, Constr. Build. Mater. 409 (2023) 133971, https://doi.org/10.1016/j.conbuildmat.2023.133971.
[4] N.K. Adomako, N. Haghdadi, S. Primig, Electron and laser-based additive manufacturing of Ni-based superalloys: A review of heterogeneities in microstructure and mechanical properties, Mater. Des. 223 (2022) 111245, https://doi.org/10.1016/j.matdes.2022.111245.
[5] H. Wu, D. Zhang, B. Yang, C. Chen, Y. Li, K. Zhou, L. Jiang, R. Liu, Microstructural evolution and defect formation in a powder metallurgy nickel-based superalloy processed by selective laser melting, J. Mater. Sci. Technol. 36 (2020) 7–17, https://doi.org/10.1016/j.jmst.2019.08.007.
[6] T. Nagahari, T. Nagoya, K. Kakehi, N. Sato, S. Nakano, Microstructure and creep properties of Ni-base superalloy IN718 built up by selective laser melting in a vacuum environment, Metals. (Basel) 10 (2020) 362, https://doi.org/10.3390/met10030362.
[7] Q. Jia, D. Gu, Selective laser melting additive manufacturing of Inconel 718 superalloy parts: Densification, microstructure and properties, J. Alloys. Compd. 585 (2014) 713–721, https://doi.org/10.1016/j.jallcom.2013.09.171.
[8] Y. Wang, L. Zhuo, M. Liu, Z. An, C. Li, E. Yin, J. Lu, X. Gong, Microstructure characteristics and surface oxidation behaviour of SLM WC/IN718 composite, Powder Metall. 65 (2022) 308–317, https://doi.org/10.1080/00325899.2021.2014649.
[9] S. He, S. Park, D.S. Shim, C. Yao, W.J. Zhang, Study on microstructure and abrasive behaviors of Inconel 718-WC composite coating fabricated by laser directed energy deposition, J. Mater. Res. Technol. 21 (2022) 2926–2946, https://doi.org/10.1016/j.jmrt.2022.10.088.
[10] J. Domitner, Z. Silvayeh, R.H. Buzolin, S. Krisam, K. Achterhold, E. Povoden-Karadeniz, C. Sommitsch, Microstructure characterization of nickel matrix composite reinforced with tungsten carbide particles and produced by laser cladding, Adv. Eng. Mater. 24 (2022) 2200463, https://doi.org/10.1002/adem.202200463.
[11] A. Aramian, N. Razavi, Z. Sadeghian, F. Berto, A review of additive manufacturing of cermets, Addit. Manuf. 33 (2020) 101130, https://doi.org/10.1016/j.addma.2020.101130.
[12] K.V. Wong, A. Hernandez, A review of additive manufacturing, ISRN Mech. Eng. 2012 (2012) 1–10, https://doi.org/10.5402/2012/208760.
[13] C.Y. Yap, C.K. Chua, Z.L. Dong, Z.H. Liu, D.Q. Zhang, L.E. Loh, S.L. Sing, Review of selective laser melting: Materials and applications, Appl. Phys. Rev. 2 (2015) 041101, https://doi.org/10.1063/1.4935926.
[14] Z. Liu, D. Zhao, P. Wang, M. Yan, C. Yang, Z. Chen, J. Lu, Z. Lu, Additive manufacturing of metals: Microstructure evolution and multistage control, J. Mater. Sci. Technol. 100 (2022) 224–236, https://doi.org/10.1016/j.jmst.2021.06.011.
[15] T. Rong, D. Gu, Formation of novel graded interface and its function on mechanical properties of WC1-x reinforced Inconel 718 composites processed by selective laser melting, J. Alloys. Compd. 680 (2016) 333–342, https://doi.org/10.1016/j.jallcom.2016.04.107.
[16] Y. Gao, H. Chen, J. Zhou, W. Tian, H. Nie, W. Wang, J. Liang, Microstructures and wear behaviors of WC particle reinforced nickel-based composites fabricated by selective laser melting, J. Manuf. Process. 95 (2023) 291–301, https://doi.org/10.1016/j.jmapro.2023.03.075.
[17] H. Zhang, Y. Wu, Y. Wang, W. Deng, G. Xu, K. Luo, J. Lu, In-situ nanoscale precipitation behavior and strengthening mechanism of WC/IN718 composites manufactured by laser powder bed fusion, Compos. B: Eng. 284 (2024) 111727, https://doi.org/10.1016/j.compositesb.2024.111727.
[18] W. Zhang, X. Lu, A. Coban, M. Cervera, M. Chiumenti, A. Sasnauskas, C. Huang, S. Yin, R.P. Babu, R. Lupoi, Powder sheet additive manufacturing of multi-material structures: Experimental and computational characterizations, Compos. B: Eng. 272 (2024) 111203, https://doi.org/10.1016/j.compositesb.2024.111203.
[19] Z. Ma, W. Liu, W. Li, H. Liu, J. Song, Y. Liu, Y. Huang, Y. Xia, Z. Wang, B. Liu, Z. Lv, G. Hu, T. Wang, T. Li, S. Liu, Y. Zhang, Additive manufacturing of functional gradient materials: A review of research progress and challenges, J. Alloys. Compd. 971 (2024) 172642, https://doi.org/10.1016/j.jallcom.2023.172642.
[20] Y. Chen, F. Liou, Additive manufacturing of metal functionally graded materials: A review, Solid Freeform Fabrication 2018: Proceedings of the 29th Annual International, pp. 1215-1231.
[21] S. Alkunte, I. Fidan, V. Naikwadi, S. Gudavasov, M.A. Ali, M. Mahmudov, S. Hasanov, M. Cheepu, Advancements and challenges in additively manufactured functionally graded materials: A comprehensive review, J. Manuf. Mater. Process. 8 (2024) 10023, https://doi.org/10.3390/jmmp8010023.
[22] R. Ghanavati, H. Naffakh-Moosavy, M. Moradi, Additive manufacturing of thin-walled SS316L-IN718 functionally graded materials by direct laser metal deposition, J. Mater. Res. Technol. 15 (2021) 2673–2685, https://doi.org/10.1016/j.jmrt.2021.09.061.
[23] A.G. Demir, B. Previtali, Multi-material selective laser melting of Fe/Al-12Si components, Manuf. Lett. 11 (2017) 8–11, https://doi.org/10.1016/j.mfglet.2017.01.002.
[24] R. Ghanavati, E. Lannunziata, E. Norouzi, S. Bagherifard, L. Iuliano, A. Saboori, Design and development of SS316L-IN718 functionally graded materials via laser powder bed fusion, Mater. Lett. 349 (2023) 134793, https://doi.org/10.1016/j.matlet.2023.134793.
[25] Y. Cao, P. Bai, F. Liu, X. Hou, Investigation on the precipitates of IN718 alloy fabricated by selective laser melting, Metals. (Basel) 9 (2019) 112, https://doi.org/10.3390/met9101128.
[26] Q. Wang, Q. Li, L. Zhang, D.X. Chen, H. Jin, J.D. Li, J.W. Zhang, C.Y. Ban, Microstructure and properties of Ni-WC gradient composite coating prepared by laser cladding, Ceram. Int. 48 (2022) 7905–7917, https://doi.org/10.1016/j.ceramint.2021.11.338.
[27] C. Garcia-Cabezon, M.A. Castro-Sastre, A.I. Fernandez-Abia, M.L. Rodriguez-Mendez, F. Martin-Pedrosa, Microstructure–hardness–corrosion performance of 17–4 precipitation hardening stainless steels processed by selective laser melting in comparison with commercial alloy, Met. Mater. Int. 28 (2022) 2652–2667, https://doi.org/10.1007/s12540-021-01155-8.
[28] V.M. Gopinath, S. Arulvel, A review on the steels, alloys/high entropy alloys, composites and coatings used in high temperature wear applications, Mater. Today: Proc. 33 (2020) 817–823, https://doi.org/10.1016/j.matpr.2020.06.495.
[29] M. Varga, S. Leroch, H. Rojacz, M.R. Ripoll, Study of wear mechanisms at high temperature scratch testing, Wear. 388–389 (2017) 112–118, https://doi.org/10.1016/j.wear.2017.04.027.
[30] M. Xie, S. Zhang, M. Li, Comparative investigation on HVOF sprayed carbide-based coatings, Appl. Surf. Sci. 273 (2013) 799–805, https://doi.org/10.1016/j.apsusc.2013.03.010.
[31] S. Mao, J. Zhang, Oxidation behaviour of Ni–Al and Ni–Cr–Al alloys in dry and wet oxygen at 750°C, High Temp. Corros. Mater. 102 (2025), https://doi.org/10.1007/s11085-025-10334-6.
[32] H. Guo, Y. Wang, M. Wang, H. Yang, B. Gu, G. Xu, E. Zhao, C. Liu, X. Gao, Microstructure, wear, and corrosion resistance of HVOF WC24-Cr3C257-NiCr19 coating, Tribol. Int. 211 (2025), https://doi.org/10.1016/j.triboint.2025.110806.
[33] S. Guo, Y. Zhao, S. Sui, P. Zhu, M. Wang, X. Hao, Y. Song, A. Guo, J. Ni, Y. Qin, X. Lin, Effect of static magnetic field on the chemical short-range order of CoCrFeMnNi high-entropy alloy prepared by laser powder bed fusion, Intermetallics. (Barking) 175 (2024) 108498, https://doi.org/10.1016/j.intermet.2024.108498.
[34] S. Gong, S. Guo, L. Liu, M. Zhang, L. Wang, Y. Ji, J. Ni, W. Yang, A. Guo, S. Liu, S. Sui, M. Wang, X. Lin, Achieving ultrafine, fully equiaxed grains and heterogeneous structures in laser powder bed fusion 316L stainless steel through in-situ alloying, Addit. Manuf. Front. 4 (4) (2025) 200243, https://doi.org/10.1016/j.amf.2025.200243.
[35] W. Yang, A. Guo, X. Sheng, R. Tang, P. Qu, S. Wang, C. Liu, L. Yin, S. Sui, S. Guo, Preparation of 316L stainless steel/WC gradient layered structures with excellent strength-elongation synergy using laser powder bed fusion, J. Manuf. Process. 133 (2025) 692–704, https://doi.org/10.1016/j.jmapro.2024.11.093.